Gondwana Research 43 (2017) 74–91

Contents lists available at ScienceDirect

Gondwana Research

journal homepage: www.elsevier.com/locate/gr

Magmatic evolution of the Tuwu–Yandong porphyry Cu belt, NW China: Constraints from geochronology, geochemistry and Sr–Nd–Hf isotopes

Bing Xiao [a,b,1], Huayong Chen [a,*], Pete Hollings [c], Jinsheng Han [a], Yunfeng Wang [a], Juntao Yang [d], Keda Cai [e]

[a] Key Laboratory of Mineralogy and Metallogeny, Guangzhou Institute of Geochemistry, Chinese Academy of Sciences, Guangzhou 510640, China
[b] Graduate University of Chinese Academy of Sciences, Beijing, China
[c] Geology Department, Lakehead University, 955 Oliver Road, Thunder Bay, ON P7B 5E1, Canada
[d] No.1 geological party Xinjiang Bureau of Geology and Mineral exploration, Changji, 831100, China
[e] Xinjiang Research Center for Mineral Resources, Xinjiang Institute of Ecology and Geography, Chinese Academy of Sciences, Urumqi 830011, China

ARTICLE INFO

Article history:
Received 30 March 2015
Received in revised form 31 August 2015
Accepted 5 September 2015
Available online 10 October 2015

Keywords:
Geochemistry
Adakitic rocks
Slab melting
Tuwu–Yandong
Eastern Tianshan mountains

ABSTRACT

The Tuwu–Yandong porphyry Cu belt is located in the Eastern Tianshan mountains in the eastern Central Asian Orogenic Belt. Petrochemical and geochronological data for intrusive and volcanic rocks from the Tuwu and Yandong deposits are combined with previous studies to provide constraints on their petrogenesis and tectonic affinity. New LA–ICP–MS zircon U–Pb ages of 348.3 ± 6.0 Ma, 339.3 ± 2.2 Ma, 323.6 ± 2.5 Ma and 324.1 ± 2.3 Ma have been attained from intrusive units associated with the deposits, including diorite, plagiogranite porphyry, quartz albite porphyry and quartz porphyry, respectively. The basalt and andesite, which host part of the Cu mineralization, are tholeiitic with high Al_2O_3, Cr, Ni and low TiO_2 contents, enriched LREEs and negative HFSE (Nb, Ta, Zr, Ti) anomalies consistent with arc magmas. Diorites are characterized by low SiO_2 content but high MgO, Cr and Ni contents, similar to those of high-Mg andesites. The parental magma of the basalt, andesite and diorite is interpreted to have been derived from partial melting of mantle-wedge peridotite that was previously metasomatized by slab melts. The ore-bearing plagiogranite porphyry is characterized by high Na_2O, Sr, Cr and Ni contents, low Y and Yb contents, low Na_2O/K_2O ratios and high Sr/Y ratios and high Mg#, suggesting an adakitic affinity. The high $\varepsilon_{Nd}(t)$ (5.02–9.16), low I_{Sr} (0.703219–0.704281) and high $\varepsilon_{Hf}(t)$ (8.55–12.99) of the plagiogranite porphyry suggest they were derived by a partial melting of the subducted oceanic crust followed by adakitic melt-mantle peridotite interaction. The quartz albite porphyry and quartz porphyry are characterized by similar Sr–Nd–Hf isotope but lower Mg# and whole-rock $(La/Yb)_N$ ratios to the plagiogranite porphyry, suggesting they were derived from juvenile lower crust, and negative Eu anomalies suggest fractionation of plagioclase. We propose that a flat subduction that started ca. 340 Ma and resulted in formation of the adakitic plagiogranite porphyry after a period of "steady" subduction, and experienced slab rollback at around 323 Ma.

1. Introduction

The Central Asian Orogenic Belt (CAOB), also referred as the Altaids or the Altaid Tectonic Collage, formed by accretion of island arcs, ophiolites, oceanic islands, seamounts, accretionary wedges, oceanic plateaux and microcontinents (Windley et al., 2007). It is the largest accretionary orogen in the world that records a long history of accretionary orogenesis from the late Proterozoic to the Mesozoic (Xiao et al., 2010, 2014; Xiao and Santosh, 2014; Xiao et al., 2015; Zhao et al., 2015). The Eastern Tianshan mountains, situated along the southern margin of the CAOB, is one of the most important Cu–Ni–Au metallogenic provinces in China (Qin et al., 2011). The Tuwu–Yandong Cu belt, located in the Eastern Tianshan mountains, Xinjiang, China, is the largest and economically most important porphyry Cu district in the province, containing ~650 million tons grading 0.46 percent Cu and 0.2 g/tonne Au, with significant amounts of Mo and Ag (Han et al., 2006; Shen et al., 2014a). The Tuwu–Yandong belt forms part of the east–west-trending Dananhu–Tousuquan island belt, which extends along the southern margin of the Turpan–Hami basin (Fig. 1). The deposits are hosted in the Carboniferous Qi'eshan Group and plagiogranite porphyry (Han et al., 2006). Since its discovery in late 1990s, many studies have been undertaken on the deposits to characterize the geology (Rui et al., 2002), alteration (Han et al., 2006), Cu mineralization (Shen et al., 2014b), geochemistry and geochronology of the plagiogranite porphyry (Hou et al., 2005; Han et al., 2014; Shen et al., 2014a,b; Wang et al., 2014), timing of mineralization (Rui et al., 2002; Zhang et al., 2010), ore-forming fluids based on inclusions (Han et al.,

* Corresponding author. Tel.: +86 13926101976.
E-mail addresses: xiaobing7960@126.com (B. Xiao), huayongchen@gig.ac.cn (H. Chen), peter.hollings@lakeheadu.ca (P. Hollings), hanjinsheng@gig.ac.cn (J. Han), yunjia512510@163.com (Y. Wang), 1179824864@qq.com (J. Yang), caikd_117@hotmail.com (K. Cai).
[1] Tel.: +86 13535579451.

http://dx.doi.org/10.1016/j.gr.2015.09.003
1342-937X/

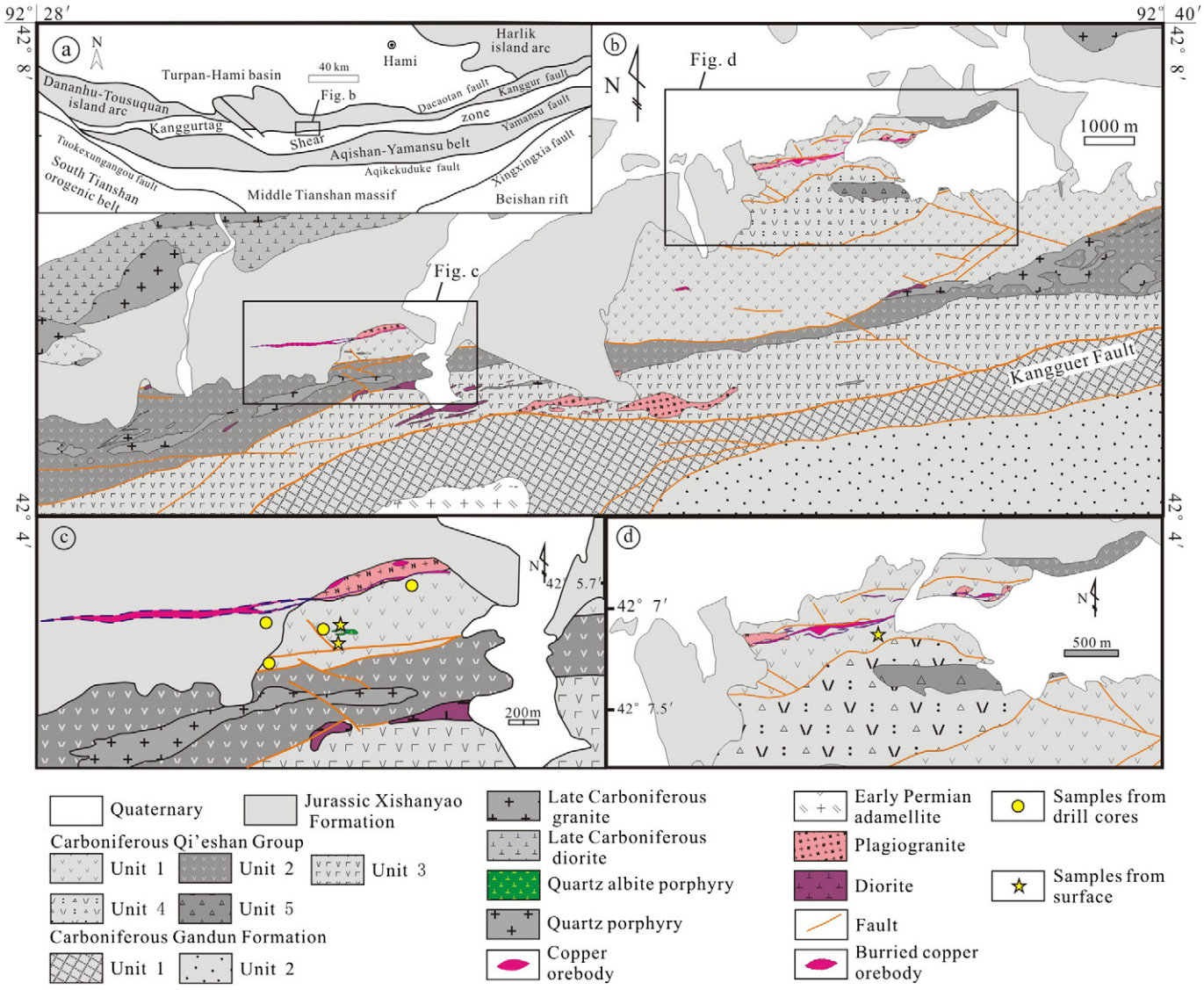

Fig. 1. (a) Tectonic subdivision of the Eastern Tianshan mountains (Han et al., 2006); (b) geologic map of the Tuwu–Yandong Porphyry Cu belt (Shen et al., 2014a); (c) geologic map of the Yandong deposit and (d) geologic map of the Tuwu deposit.

2006; Zhang et al., 2010) and C-H-O-S stable isotopes (Han et al., 2006; Zhang et al., 2010). To date, however, little research has focused on the geochronology and petrogenesis of the diorite, quartz albite porphyry and quartz porphyry within the deposits, which can, together with the well-documented ore-bearing plagiogranite porphyry, provide critical information on the magmatic evolution of the Tuwu–Yandong Cu belt and the genesis of Cu mineralization.

In this study, we present new field observations, petrography, geochemistry, and in situ zircon U–Pb–Hf laser-ablation inductively coupled plasma mass spectrometer (LA–ICP–MS) analyses, as well as Sr–Nd isotope analyses for the plagiogranite porphyry, diorite, quartz albite porphyry, quartz porphyry and volcanic rocks in the Tuwu and Yandong deposits. These results will be used to constrain the timing and petrogenesis of the intrusions, and develop a model for the magmatic evolution of this important porphyry Cu belt.

2. Regional geology

The Eastern Tianshan mountains have been the focus of many previous studies of petrology, geochemistry, metallogenesis, geochronology and tectonics (Allen et al., 1993; Ma et al., 1997; Gao et al., 1998; Qin et al., 2002; Rui et al., 2002; Shu et al., 2004; Li et al., 2005; Windley et al., 2007; Mao et al., 2008; Gao et al., 2009; Xiao et al., 2009; Su et al., 2011; Chen et al., 2012b; Xiao et al., 2013). These studies have subdivided the Eastern Tianshan mountains from south to north into the Middle Tianshan massif, the Aqishan–Yamansu belt, the Kanggur shear zone and the Dananhu–Tousuquan island arc, with a series of approximately east–west-trending faults defining the boundaries, including the Aqikekuduke, Yamansu, Kanggur and Dacaotan faults (Fig. 1a).

The Middle Tianshan massif, bound by the Aqikekuduke Fault in the north, is characterized by calc-alkaline basaltic to andesitic volcanic and volcaniclastic rocks, minor I-type granites and granodiorites, and Precambrian basement rocks. The Aqishan–Yamansu belt, located between the Aqikekuduke Fault and the Yamansu Fault (Fig. 1a), is composed of lavas, volcaniclastic rocks and terrigenous clastic sedimentary rocks interbedded with limestones (Xiao et al., 2004). Several iron ore deposits have been recognized in the volcanic rocks, including the Yamansu, Kumutag, Bailingshan and Hongyuntan deposits (Hou et al., 2014). The Kanggur shear zone, located between the Yamansu Fault and the Kanggur Fault, contains marine lavas and pyroclastic rocks. Most rocks of the Kanggur shear zone have undergone greenschist facies

metamorphism and ductile deformation (Xiao et al., 2004) and are host to both gold (Chen et al., 2012a) and Cu–Ni sulfide deposits (Mao et al., 2008). The Dananhu–Tousuquan belt comprises Devonian to Carboniferous volcanic and intrusive rocks, which host significant porphyry Cu deposits, such as the Tuwu, Yandong, Linglong, Chihu and Fuxing deposits (Wu et al., 2006; Shen et al., 2014a).

3. Deposit geology

The Tuwu and Yandong Cu deposits are located in the Dananhu–Tousuquan island belt, about 1–4 km north of the Kanggur Fault (Fig. 1b). The main lithostratigraphic units in the region are the Carboniferous Qi'eshan Group and the Jurassic Xishanyao Formation (Fig. 1b). In the vicinity of the deposits, the Qi'eshan Group is east striking and dips to the south at 43° to 63°, generally with well-developed schistosity (Shen et al., 2014a). It is typically 600–2000 m thick and can be divided into five units. The diorite porphyrite defined in the literature (Shen et al., 2014a,b) have similar mineral compositions and geochemical features with the andesite in the Qi'eshan Group, without intrusive contact relationships between them. Therefore, we incorporate the so-called diorite porphyrite into the Qi'eshan Group. The lowermost unit is composed of basalt intercalated with andesite, dacite and tuff, which are overlain by pebbly sandstones intercalated with basalt and andesite. The third unit is composed of pebbly sandstone intercalated with volcaniclastic breccia which are overlain by lava breccias and conglomerates and the uppermost polymictic conglomerates. The basalt flows are generally porphyritic with phenocrysts of plagioclase with minor augite, biotite and amphibole, and a groundmass of plagioclase with minor magnetite (Fig. 2a and b). The andesite is also porphyritic but the phenocrysts and groundmass are typically plagioclase with minor amphibole and quartz (Fig. 2c and d). Previous studies indicate that the basalt and andesite of the Qi'eshan Group formed during the Early Carboniferous, but the tectonic setting remains controversial (Xia et al., 2004; Hou et al., 2006; Shen et al., 2014b). Some studies have suggested that these volcanic rocks are associated with subduction (Hou et al., 2006; Shen et al., 2014b), but others suggest that they are rift-related (Xia et al., 2004). The Jurassic Xishanyao Formation is mainly composed of sandstone, siltstone, mudstone, and conglomerate, and is separated from the Qi'eshan Group by an angular unconformity (Wang et al., 2014).

In the vicinity of the deposits, the Qi'eshan Group is intruded by the diorites, plagiogranite porphyry, quartz albite porphyry and quartz

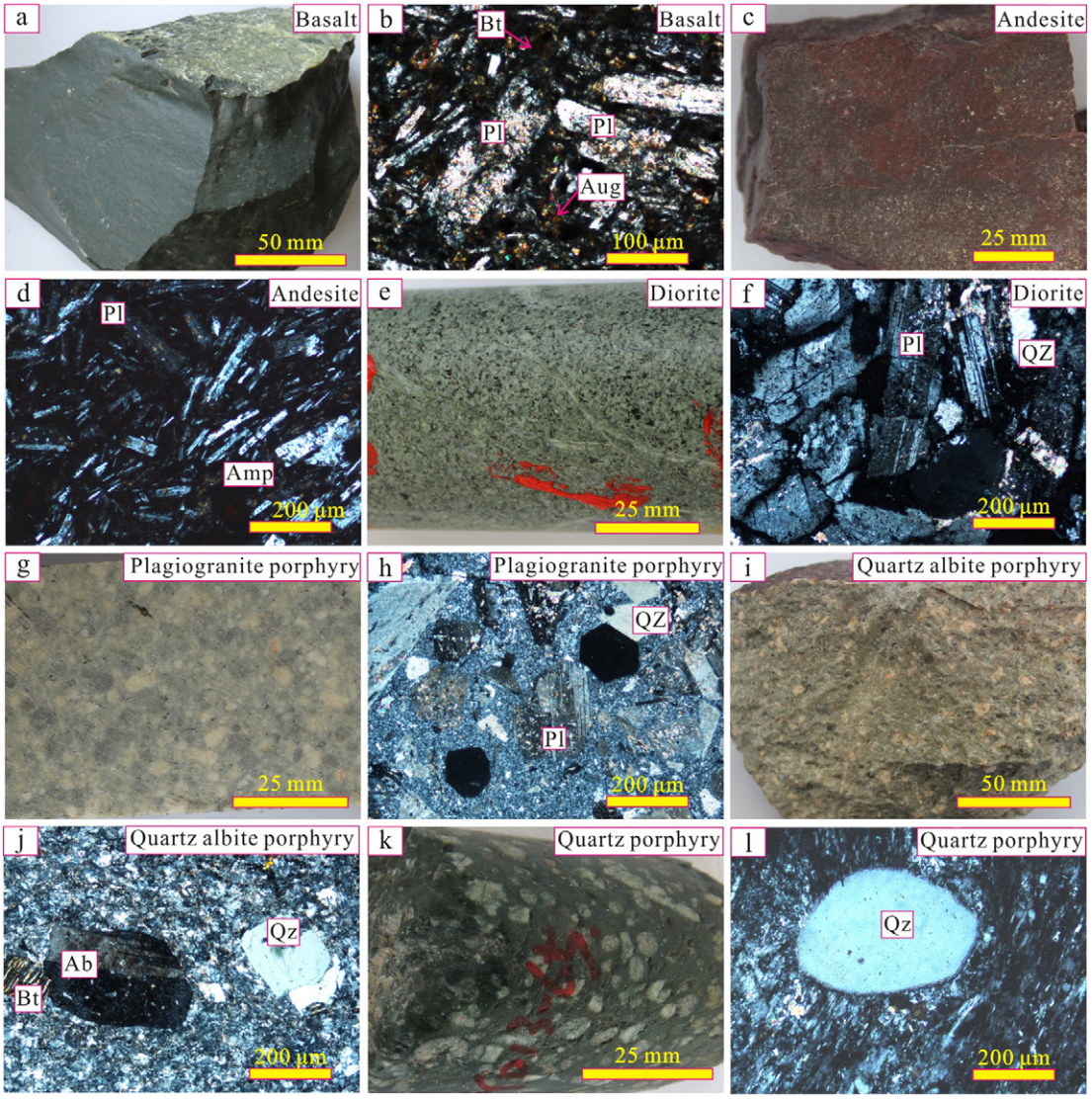

Fig. 2. Photographs showing the mineralogy and textural features of representative samples from the Tuwu and Yandong deposits. (a and b) basalt; (c and d) andesite; (e and f) diorite; (g and h) plagiogranite porphyry; (i and j) quartz albite porphyry; (k and l) quartz porphyry. Abbreviations: Qz, quartz; Pl, plagioclase; Ab, albite; Bt, biotite; Aug, augite; Amp, amphibole.

porphyry. The diorite is composed of plagioclase (>90%) and amphibole (5–10%) with accessory zircon (Fig. 2e and f). The widely-distributed and ore-bearing plagiogranite porphyry, also referred to as tonalite (Wang et al., 2014), is massive and porphyritic in texture. It contains 35–45% plagioclase, 25–35% quartz and about 5% biotite with accessory zircon and apatite (Fig. 2g and h). The less-common quartz albite porphyry is also massive and porphyritic in texture (Fig. 2i and j). It contains 30–40% albite and 30–45% quartz with accessory zircon and apatite. The quartz porphyry, mainly occurring at south of the Yandong deposit (Fig. 1c), is also porphyritic in texture, but the phenocrysts are mainly quartz (Fig. 2k and l).

The Tuwu and Yandong Cu deposits are mainly controlled by EW-, NW- and NE-trending faults (Fig. 1c-d). The mineralization is dominated by disseminated, veinlet-like and veinlet-disseminated types with no distinct boundary between the ore bodies and the country rock. Using a nominal cut-off grade of 0.50% Cu to outline the orebody, the main orebody in the Yandong deposit extends for over 3000 m in length and is 10–50 m wide (Fig. 1c). The Tuwu deposit comprises two main orebodies. Orebody I is 1400 m long, 10 to 130 m thick, and dips toward 180° at angles of 65–80°, whereas orebody II extends for over 1000 m and is 10 to 80 m in width (Fig. 1d; Zhang et al., 2006). In the Tuwu deposit, 70% of the Cu ore is hosted in the Qi'eshan Group and 30% in the plagiogranite porphyry whereas in the Yandong deposit 80% of the Cu ore is hotsted in the plagiogranite porphyry and 20% in the Qi'eshan Group. Ore minerals in the Tuwu and Yandong deposits are dominated by pyrite, chalcopyrite and molybdenite with minor bornite, chalcocite, magnetite, sphalerite, and galena. Gangue minerals are mainly composed of quartz, sericite, chlorite, epidote, anhydrite, gypsum, muscovite, biotite, apatite, sphene, dolomite, actinolite, barite, albite and calcite. Previous studies have shown that propylitic and phyllic alteration are mostly widespread in the Tuwu and Yandong deposits with the main ore horizons within the phyllic zone (Han et al., 2006; Shen et al., 2014a,b). Compared to the Tuwu deposit, potassic alteration is less developed in the Yandong deposit. Fluid inclusions and C-H-O-S stable isotopes indicate that ore fluids were mainly magma derived (Han et al., 2006; Zhang et al., 2010).

4. Samples and analytical methods

Thirty samples from the Tuwu–Yandong deposits were collected for petrographic observation during this study. The fourteen least altered samples were selected for whole-rock geochemical analysis by X-ray fluorescence (XRF) and inductively coupled plasma–mass spectrometry (ICP–MS). Four of these fourteen samples were also chosen for zircon U–Pb–Hf isotope dating. Three samples were selected for Sr–Nd isotopic analysis.

Major and minor elements geochemical analyses were undertaken at ALS Mineral/ALS Chemex (Guangzhou) Co Ltd at Guangzhou, China. Major oxide concentrations were measured by XRF spectrometer. Fused glass disks with Lithium Borate were used and the analytical precisions were better than ± 0.01%, estimated from repeated analyses of the standards GSR-2 and GSR-3. Trace element concentrations were determined by inductively coupled plasma mass spectrometry (ICP–MS). Analyses of USGS rock standards (BCR-2, BHVO-1 and AGV-1) indicate precision and accuracy better than ± 5% for trace elements. Detailed analytical method and procedure is given in Zhou et al. (2014).

Four zircon samples (diorite, plagiogranite porphyry, quartz albite porphyry and quartz porphyry) were prepared for zircon U–Pb–Hf analysis. Prior to analysis, zircon grains were separated using standard density and magnetic separation techniques before hand-picking under a binocular microscope. Representative zircon grains were mounted in epoxy resin and polished to expose the centers of individual crystals. Zircon morphology and internal structures were imaged using a JEOL JXA-8100 Superprobe at the Guangzhou Institute of Geochemistry, Chinese Academy of Sciences (GIG CAS); these images were used as guides during LA–ICP–MS analysis. In situ U–Pb dating and Lu–Hf isotopic analysis of zircon was undertaken at the State Key Laboratory of Isotope Geochemistry, GIG CAS.

LA–ICP–MS zircon U–Pb dating and trace element analyses were synchronously conducted on an Agilent 7500 ICP–MS equipped with a 193 nm laser. Laser ablation was operated at a constant energy of 80 mJ, with a repetition rate of 8 Hz and a spot diameter of 31 μm. The zircon Temora standard was used for external standardization, the Qinghu standard and NIST SRM 610 glass were used to optimize the machine. Repeated analyses of standard zircon yielded $^{206}Pb/^{238}U$ age of 416.9 ± 2.8 Ma for Temora (MSWD = 0.1, n = 22) and 160.6 ± 2.0 Ma for Qinghu (MSWD = 1.4, n = 9), which were in good agreement with the recommended Temora $^{206}Pb/^{238}U$ age of 416.8 ± 1.1 (Y.S. Liu et al., 2010) and Qinghu $^{206}Pb/^{238}U$ age of 159.5 ± 0.2 Ma (Li et al., 2013), respectively. The operating conditions for the laser ablation system and the ICP–MS instrument, and the data reduction techniques are as used by (Li et al., 2012). Concordia diagrams and weighted mean calculations were constructed using Isoplot/Ex program 3.0 (Ludwig, 2003).

In situ zircon Hf isotopic analyses were conducted using a Neptune MC–ICPMS, equipped with a 193 nm laser. All zircon grains were analyzed using a single-spot ablation mode at a spot size of 44 μm. The Penglai zircon standard was used for external standardization. The obtained $^{176}Hf/^{177}Hf$ isotopic ratios of standard zircon grains were 0.282880 ± 0.000011 (2σ, n = 10) for Penglai, which were in good agreement with the recommended Penglai $^{176}Hf/^{177}Hf$ isotopic ratios of 0.282906 ± 0.000006 (Li et al., 2010). Detailed operating conditions for the laser ablation system, the MC–ICP–MS instrument, and the analytical method are given by (Tang et al., 2012).

Sr and Nd isotopic analyses were performed on a Micromass Isoprobe multi-collector ICPMS at the GIG CAS, using analytical procedures of Tang et al. (2012). Sr and REE were separated using cation columns, and Nd fractions were further separated by HDEHP-coated Kef columns. Measured $^{87}Sr/^{86}Sr$ and $^{143}Nd/^{144}Nd$ ratios were normalized to $^{86}Sr/^{88}Sr = 0.1194$ and $^{146}Nd/^{144}Nd = 0.7219$, respectively. The reported $^{87}Sr/^{86}Sr$ and $^{143}Nd/^{144}Nd$ ratios were adjusted to the NBS SRM 987 standard of $^{87}Sr/^{86}Sr = 0.71025$ and the Shin Etsu JNdi-1 standard of $^{143}Nd/^{144}Nd = 0.512115$.

5. Hydrothermal alterations and element mobility

All the samples were collected from the Tuwu and Yandong deposits and have undergone various degrees of hydrothermal alteration based on petrographic observations (Fig. 2) and high LOI in some samples (Supplementary Appendix 1). Consequently it is very necessary to evaluate the effects of hydrothermal alteration on major and trace elements prior to discuss classification, petrogenesis and tectonic setting.

It is generally accepted that Zr is the most immobile element in low-grade metamorphism and alteration process (Guo et al., 2013). Hence, correlations between Zr and other elements can be used to discriminate the mobility of elements during post-magmatic processes (Polat et al., 2002; Liu et al., 2012). All of the samples analyzed during this study show scattered trends between the alkali metals (such as Na; Fig. 3a) and LILEs (such as Rb; Fig. 3b) with Zr, whereas the high field strength elements (such as Ti and Nb; Fig. 3c and f), transition element (such as Fe; Fig. 3d), REEs (such as Sm; Fig. 3e), are strongly correlated with Zr. Moreover, Fe, Ti, Mg, P, Al and Ca exhibit good linear relationships with SiO_2 in the Harker diagram (Fig. 4), suggesting that these elements were essentially immobile during hydrothermal alteration and can be used for the petrogenetic interpretation and tectonic discriminations.

6. Results

6.1. Whole-rock geochemistry

Major and trace element data of the representative plutons in the Tuwu and Yandong deposits are presented in Supplementary Appendix

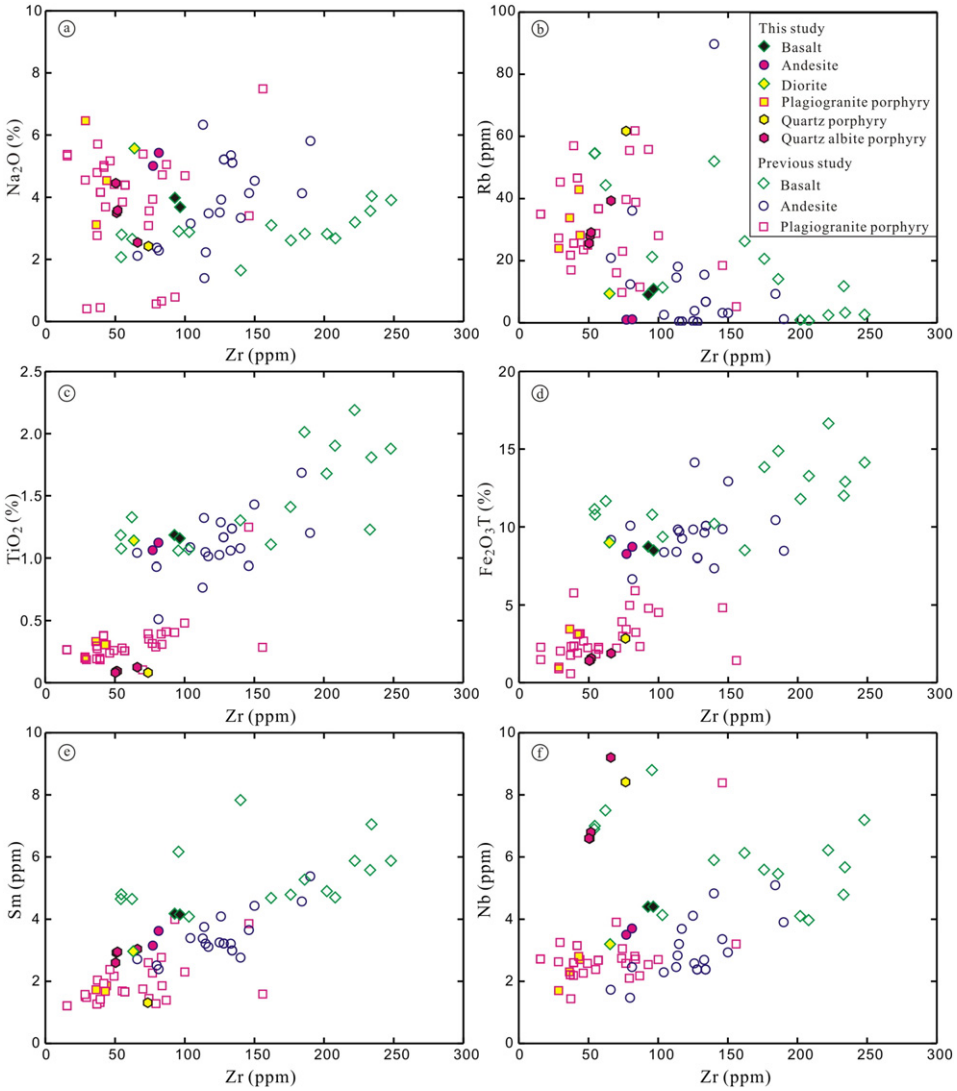

Fig. 3. Covariation diagrams of Zr versus selected alkali metals (such as Na), LILEs (such as Rb), HFSE (such as Ti and Nb), transition element (such as Ti), REEs (such as Sm) for whole-rock samples. The data for previous studies are from Han et al. (2006), Li et al. (2006), Shen et al. (2014a), Shen et al. (2014b), Wang et al. (2014), Zhang et al. (2006), and Zhang et al. (2010).

1. Since K and Na display significant remobilization, standard classifications such as the total alkali versus SiO_2 and the K_2O–SiO_2 diagram cannot be employed, whereas the HFSE and REE are immobile during metamorphism and alterations. Consequently, we use the Zr/TiO_2–SiO_2 diagram to classify the Tuwu and Yandong igneous rocks. In the Zr/TiO_2 vs. SiO_2 diagram (Winchester and Floyd, 1977), the basalt, andesite, diorite, plagiogranite porphyry, quartz albite porphyry and quartz porphyry correspondingly plot in the Sub-alkaline basalt, Andesite, Andesite, Rhyodacite/Dacite, Rhyolite and Rhyolite fields (Fig. 5a), respectively, which is consistent with petrography observation. The basalt has basaltic compositions with a restricted range of SiO_2 (from 43.0 to 52.2 wt.%), relatively high contents of Al_2O_3 (14.1–19.2 wt.%) and low TiO_2 (1.02–2.07 wt.%), Fe_2O_3T (8.12–15.74 wt.%) and P_2O_5 (0.17–0.67 wt.%). The diorite show similar geochemistry features with the andesite, which shows SiO_2, Al_2O_3, Fe_2O_3T and TiO_2 contents of 51.2–62.5 wt.%, 13.5–18.9 wt.%, 6.26–13.41 wt.% and 0.48–1.66 wt.%, respectively. The plagiogranite porphyry display SiO_2 = 64.3–74.4 %, Al_2O_3 = 12.3–17.7 %, MgO = 0.46–2.2 % and K_2O = 0.94–3.49 %. They have Mg# (Mg-numbers) ranging from 16 to 63 (mostly between 40 and 63). In the SiO_2 versus Mg# diagram, the plagiogranite porphyry mainly plots within the Subducted slab-derived adakites field (Fig. 5b). The quartz porphyry show similar geochemistry features to the quartz albite porphyry, with high concentrations of SiO_2 (65.5–76.3 wt.%) and Na-enrichment (Na_2O = 2.45–4.35 wt.%, Na_2O/K_2O = 2.6–4.0), but low concentrations of TiO_2 (0.08–0.12 wt.%), Fe_2O_3T (1.38–1.82 wt.%), MnO (0.08–0.09 wt.%), MgO (0.47–0.60 wt.%), and P_2O_5 (0.03–0.04 wt.%) and moderate Mg# (34–44).

All the intrusive and volcanic rocks display negative Nb, Ta, P and Ti anomalies, and enrichment in the large ion lithophile elements (LILE) on the primitive-mantle-normalized multi-element variation diagrams. They are light REE (LREE)-enriched and heavy REE (HREE)-depleted (Fig. 6). Compared with the basalt, andesite and diorite, however, the plagiogranite porphyry, quartz albite porphyry, and quartz porphyry show greater depletions in P and Ti. In addition, the quartz albite porphyry and quartz porphyry show significantly negative Eu anomalies.

6.2. Zircon trace elements

Zircon trace elements of the studied samples from the Tuwu and Yandong deposits are presented in Supplementary Appendix 2. Zircon grains in this study are enriched in HREE relative to LREE, with positive

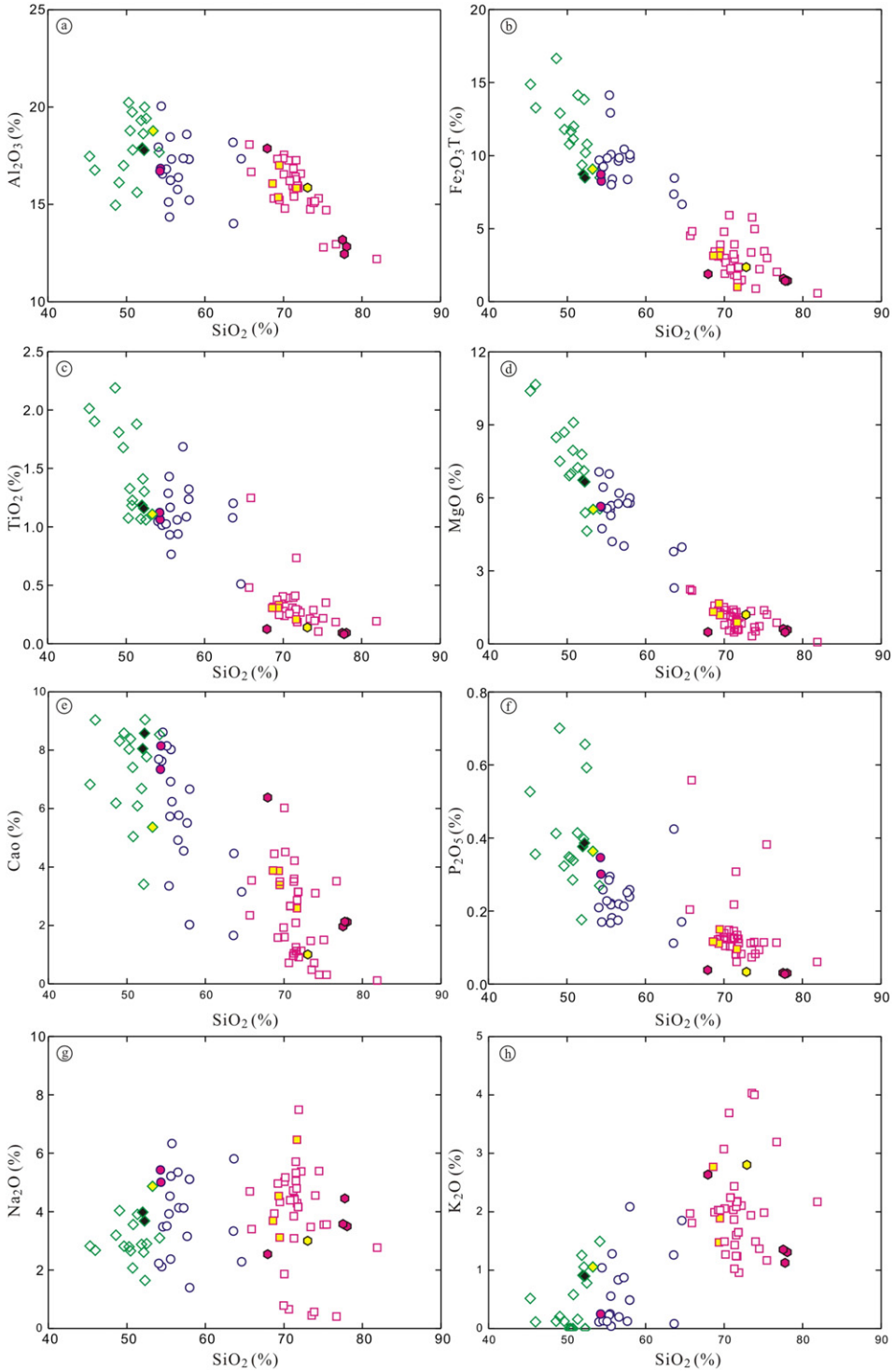

Fig. 4. Harker diagrams for samples analyzed from previous and this study. Legends same as for Fig. 3.

Ce and negative Eu anomalies (Fig. 7), which are common features of magmatic zircon grains in igneous rocks (Hoskin and Schaltegger, 2003). The zircon Ce^{4+}/Ce^{3+} ratios and Ti-in-zircon thermometer can be used to determine magma forming temperatures and the oxidation state (Ballard et al., 2002; Liang et al., 2006; Ferry and Watson, 2007). Zircon Ce^{4+}/Ce^{3+} ratios range from 8 to 208 (avg. 69, n = 21) in the quartz albite porphyry and 3 to 69 (avg. 20, n = 19) in the quartz porphyry (Fig. 8a). Calculated Ti-in-zircon temperatures vary from 638 to 823 °C (avg. 726 °C, n = 21) in the quartz albite porphyry and 667 to 948 °C (avg. 764 °C, n = 19) in the quartz porphyry (Fig. 8b). Zircon from the quartz albite porphyry and quartz porphyry both show a wide range of δEu (Fig. 8c; 0.09–0.65). Compared with the quartz albite porphyry and quartz porphyry, the diorite and plagiogranite porphyry show higher zircon Ce^{4+}/Ce^{3+} ratios (Fig. 8a) and a narrower range of δEu (Fig. 8c). The diorite has higher Ti-in-zircon temperatures (765 to 812 °C, avg. 792 °C, n = 6) than the plagiogranite porphyry, quartz

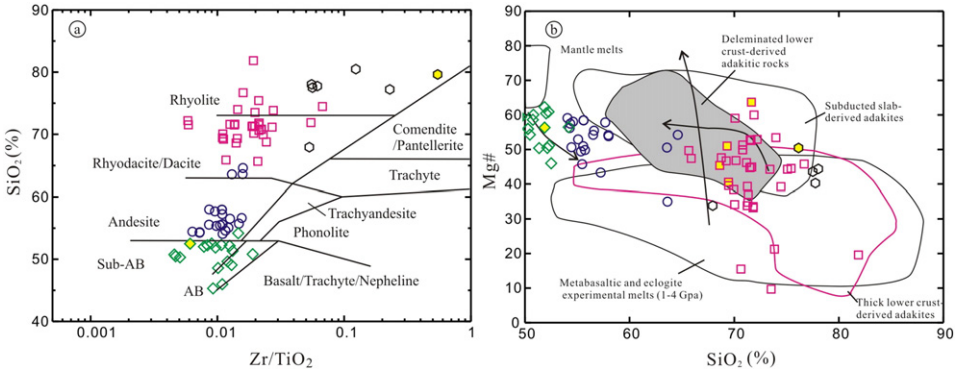

Fig. 5. (a) Zr/TiO_2versus SiO_2 classification diagram, after Winchester and Floyd (1977); (b) SiO_2 versus Mg#, after Wang et al. (2006). Legends same as for Fig. 3.

albite porphyry and quartz porphyry. In the T vs. logfO_2 diagram (Trail et al., 2011; Sun et al., 2015), the plagiogranite porphyry and diorite mainly plot between the fayalite-magnetite-quartz (FMQ) buffer curve and the magnetite–haematite (MH) buffer curve, while the quartz albite porphyry and quartz porphyry mainly plot between FMQ and the iron–wüstite (IW) buffer curve (Fig. 8d).

6.3. Zircon U–Pb–Hf isotopic systematics

The representative CL images of zircon grains are shown in Fig. 9 with zircon U–Pb analyses listed in Fig. 10 and Supplementary Appendix 3. Lu-Hf isotopic analyses are given in Table 1 and shown in Fig. 11. In situ Hf isotope analyses were undertaken on the same spots used for LA–ICP–MS zircon U–Pb dating in order to match the Hf isotope data with U–Pb ages.

Ten zircon grains separated from the diorite (sample YD13-91) are generally transparent and prismatic with lengths of 50–100 μm and widths of 30–60 μm, and show oscillatory magmatic zoning (Fig. 9a). Six of these grains yielded concordant $^{206}Pb/^{238}U$ ages ranging from 351.8 to 345.2 Ma (Supplementary Appendix 3), returning a weighted mean $^{206}Pb/^{238}U$ age of 348.3 ± 6.0 Ma (2σ; n = 6) with a MSWD value of 0.13 (Fig. 10a). These analyses mostly show markedly positive Ce anomalies and negative Eu anomalies (Fig. 7a) and high Th/U ratios (0.53–0.78), indicative of a magmatic origin (Hoskin and Schaltegger, 2003). Therefore, we consider this age to indicate the timing of crystallization of the diorite.

Zircon grains from the plagiogranite porphyry (sample YD13-114-1) are generally euhedral, prismatic, with elongation ratios ranging from 1.5 to 3.8. The zircon grains display evidently oscillatory magmatic zoning on CL images, indicative of magmatic genesis (Fig. 9b). A total of twenty-five analyses of zircon grains separated from sample YD13-114-1 were undertaken. Excluding one discordant analysis, the remaining twenty-four analyses plot along a concordia line. Twenty-two of these analyses yielded concordant $^{206}Pb/^{238}U$ ages ranging from 342.4 to 335.1 Ma (Supplementary Appendix 3), returning a weighted mean $^{206}Pb/^{238}U$ age of 339.3 ± 2.2 Ma (2σ; n = 22) with a MSWD value of 0.14 (Fig. 10b); these zircon show positive Ce anomalies and negative Eu anomalies (Fig. 7b), and possess high Th/U ratios (0.17–0.69), indicative of a magmatic origin. Therefore, we consider this age to indicate the timing of crystallization of the plagiogranite porphyry. Two analysis (#21 and #25) on two zircon grains with Th/U ratios of 0.41 and 0.42 yield $^{206}Pb/^{238}U$ ages of 364.4 ± 7.8 Ma and 365.9 ± 7.1 Ma, respectively, suggesting that these zircon grains are inherited. Ten zircon Lu-Hf isotopic analyses from sample YD13-114 yielded $^{176}Yb/^{177}Hf$ values of 0.034555–0.060595, and $^{176}Hf/^{177}Hf$ values of 0.282815–0.282938, but with low $^{176}Lu/^{177}Hf$ values of 0.001422–0.002576 (Table 1). These analyses yield $\varepsilon_{Hf}(t)$ values of 8.55 to 12.99, single-stage Hf isotopic model (T_{DM1}) ages of 633–451 Ma, and two-stage Hf isotopic model (T_{DM2}) ages of 800–516 Ma. All the other analyses plot between depleted mantle (DM) and CHUR lines in a $\varepsilon_{Hf}(t)$ vs. age diagram (Fig. 11a). The inherited zircon grains that yielded $^{206}Pb/^{238}U$ ages of 364.4 ± 7.8 Ma and 365.9 ± 7.1 Ma have $\varepsilon_{Hf}(t)$ values of 12.74 and 11.05, and T_{DM2} ages of 552 Ma and 661 Ma, respectively.

Zircon grains from the quartz albite porphyry (sample YD13-1) are generally transparent, euhedral or subhedral with a range in length to width ratios of 2.0 to 5.0, and contain oscillatory magmatic zoning indicative of magmatic genesis (Fig. 9c). A total of twenty-five analyses of zircon grains separated from sample YD13-1 were undertaken. Excluding two discordant analyses, the remaining twenty-three analyses plot along a concordia line. Twenty-one of these analyses yield concordant $^{206}Pb/^{238}U$ ages ranging from 327.9 to 317.8 Ma (Supplementary Appendix 3) and a weighted mean $^{206}Pb/^{238}U$ age of 323.6 ± 2.5 Ma (2σ; n = 21) with a MSWD value of 0.13 (Fig. 10c). The zircon grains show positive Ce anomalies and negative Eu anomalies (Fig. 7c), and high Th/U ratios range of 0.47–1.50, indicative of a magmatic origin. Therefore, we consider this age to indicate the timing of crystallization of the quartz albite porphyry. Two analysis (#4 and #22) on two zircon grains with Th/U ratios of 0.32 and 0.60 yielded $^{206}Pb/^{238}U$ ages of 359.0 ± 5.7 Ma and 360.6 ± 7.0 Ma, respectively. These zircon grains are inherited. Ten zircon Lu-Hf isotopic analyses from sample YD13-1 yielded $^{176}Yb/^{177}Hf$ and $^{176}Hf/^{177}Hf$ values of 0.036489–0.080633 and 0.282806–0.282908, but low $^{176}Lu/^{177}Hf$ values of 0.001473–0.003300 (Table 1). These analyses yield $\varepsilon_{Hf}(t)$ values of 7.61 to 11.64, single-stage Hf isotopic model (T_{DM1}) ages of 674–494 Ma, and two-stage Hf isotopic model (T_{DM2}) ages of 849–592 Ma. All the other analyses plot between depleted mantle (DM) and CHUR lines in a $\varepsilon_{Hf}(t)$ vs. age diagram (Fig. 11b). The inherited zircon that yielded a $^{206}Pb/^{238}U$ age of 360.6 ± 7.0 Ma has a $\varepsilon_{Hf}(t)$ value of 11.88 and a T_{DM2} age of 604 Ma.

Zircon grains from the quartz porphyry (sample YD13-165) are generally transparent, euhedral or subhedral with a range in length to width ratios 1.0 to 4.0, and contain oscillatory magmatic zoning (Fig. 9d) indicative of a magmatic genesis. A total of twenty analyses of zircon grains separated from sample YD13-165 were undertaken. All analyses plot along a concordia line (Fig. 10d). Nineteen of these analyses yielded concordant $^{206}Pb/^{238}U$ ages ranging from 326.8 to 323.1 Ma (Supplementary Appendix 3), returning a weighted mean $^{206}Pb/^{238}U$ age of 324.1 ± 2.3 Ma (2σ; n = 19) with a MSWD value of 0.15; these zircon grains show markedly positive Ce anomalies and negative Eu anomalies (Fig. 7d), and possess high Th/U ratios (0.28–1.70), indicative of a magmatic origin. Therefore, we consider this age to indicate the timing of crystallization of the quartz porphyry. One analysis (#8) on one zircon grain with Th/U ratios of 1.00 yielded $^{206}Pb/^{238}U$ ages of 362.9 ± 8.4 Ma Which means it is inherited.

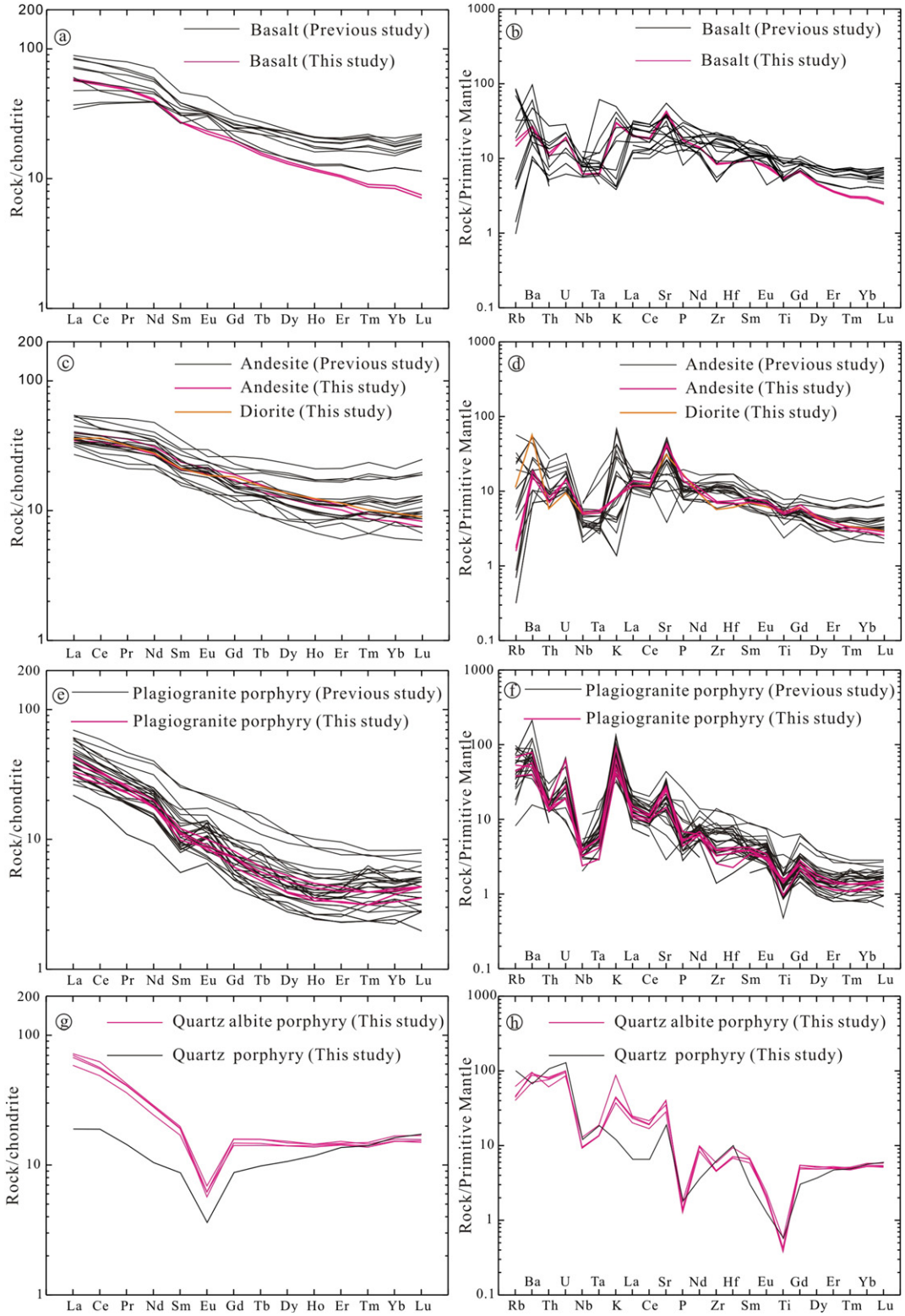

Fig. 6. Chondrite-normalized REE and Primitive-mantle-normalized diagrams for samples from the Tuwu and Yandong deposits; chondrite and primitive mantle values are from Sun and McDonough (1989).

Eleven zircon Lu-Hf isotopic analyses from sample YD13-1 yielded $^{176}Yb/^{177}Hf$ and $^{176}Hf/^{177}Hf$ values of 0.041256–0.102302 and 0.282823–0.282893, but low $^{176}Lu/^{177}Hf$ values of 0.001679–0.003985 (Table 1). These analyses yield $\varepsilon_{Hf}(t)$ values of 8.13 to 10.86, single-stage Hf isotopic model (T_{DM1}) ages of 658–529 Ma, and two-stage Hf isotopic model (T_{DM2}) ages of 817–640 Ma. All the other analyses plot between depleted mantle (DM) and CHUR lines in a $\varepsilon_{Hf}(t)$ vs. age diagram (Fig. 11c). The inherited zircon that yielded a $^{206}Pb/^{238}U$ age of 362.9 ± 8.4 Ma has a $\varepsilon_{Hf}(t)$ value of 9.84 and a T_{DM2} age of 736 Ma.

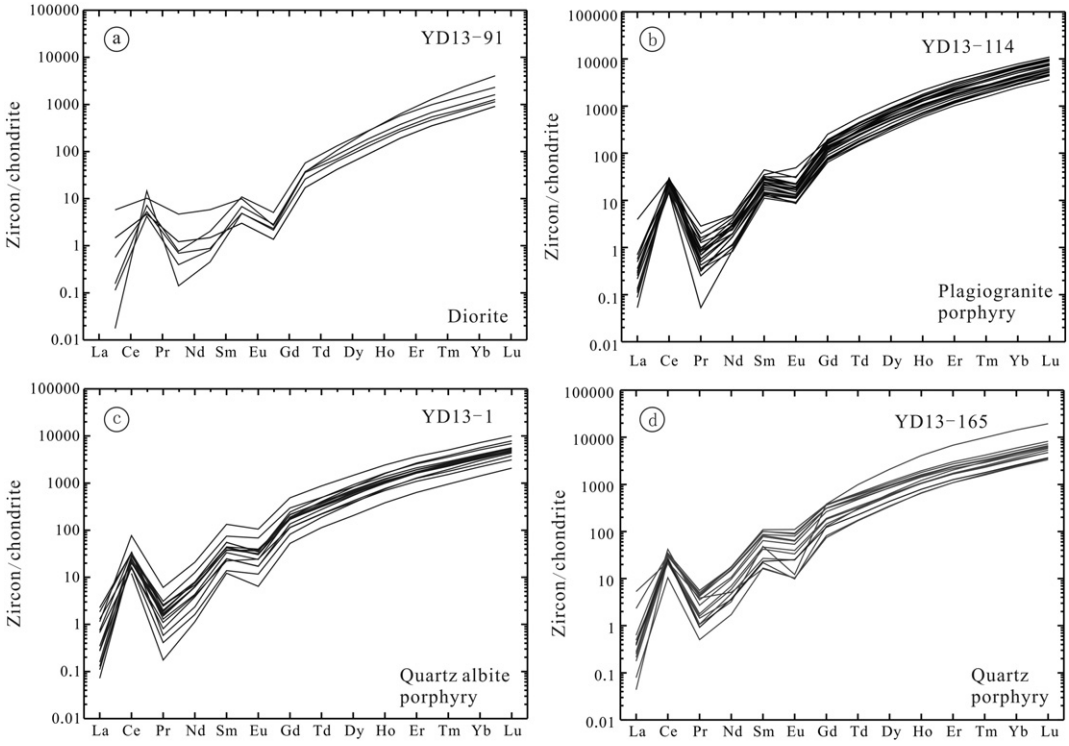

Fig. 7. Chondrite-normalized REE patterns of analyzed zircon.

6.4. Sr–Nd isotope

Whole–rock Rb–Sr and Sm–Nd isotope compositions of the studied samples from the Tuwu and Yandong deposits are presented in Table 2. The initial $^{87}Sr/^{86}Sr$ ratios and $\varepsilon_{Nd}(t)$ values were calculated based on the zircon U–Pb ages. All the samples have relatively homogeneous Nd isotopic compositions with $^{143}Nd/^{144}Nd$ ratios of 0.512724 to 0.512977, corresponding to $\varepsilon_{Nd}(t)$ ranging from 5.02 to 9.85. Compared with the basalt and andesite, the plagiogranite and quartz albite porphyry samples have higher $^{87}Rb/^{86}Sr$ ratios (0.08–1.05) and lower $^{147}Sm/^{144}Nd$

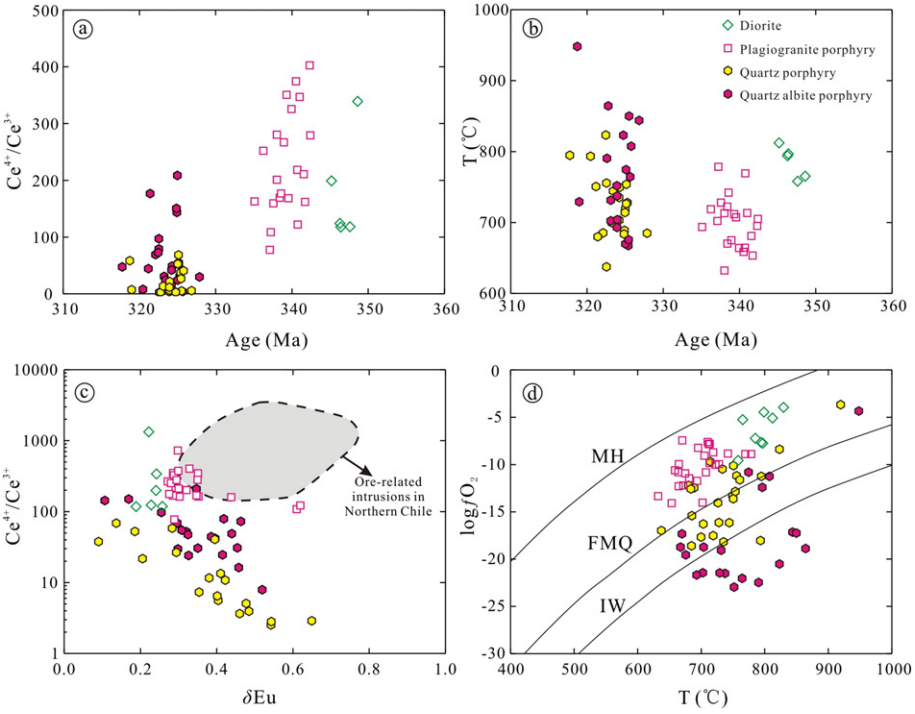

Fig. 8. (a) Zircon age vs. Ce^{4+}/Ce^{3+} ratios; (b) zircon age vs. T; (c) Zircon δEu vs. Ce^{4+}/Ce^{3+} ratios and (d) T vs. logfO_2 (Trail et al., 2012; Sun et al., 2015). The data for ore-related intrusions in Northern Chile are from Muñoz et al. (2012).

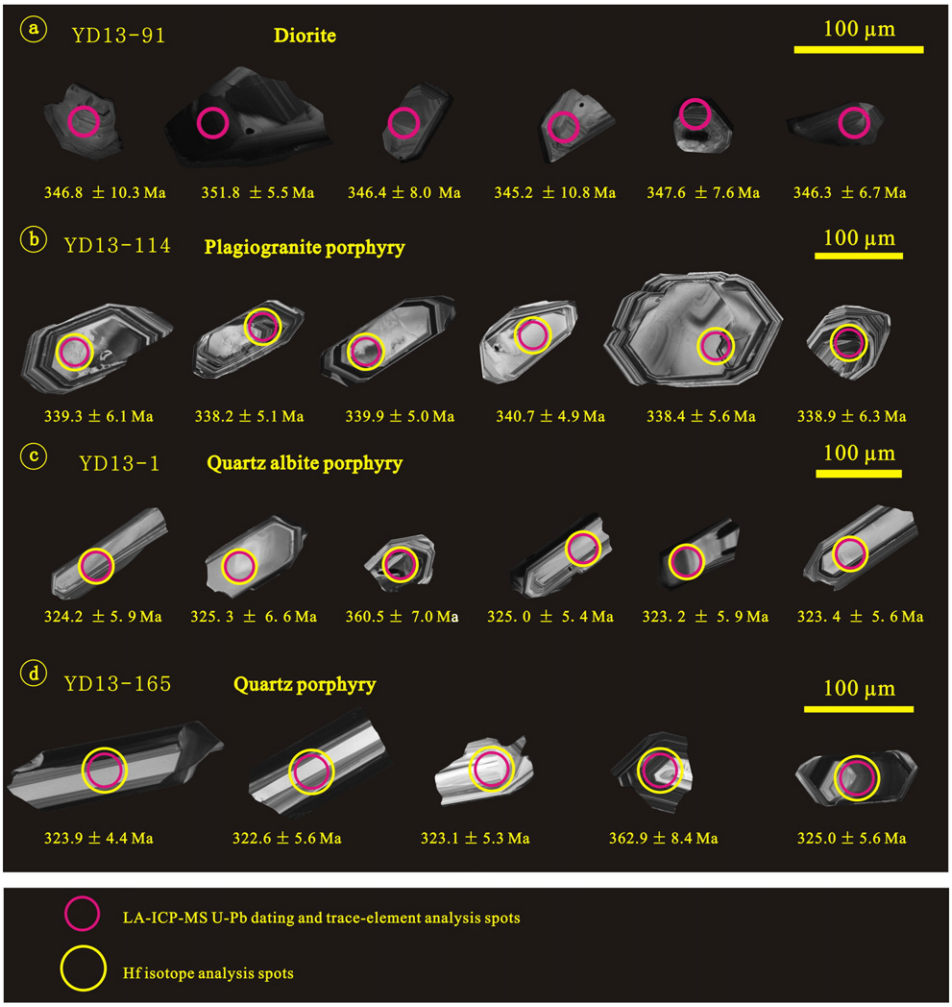

Fig. 9. Cathodoluminescence images of representative zircon grains showing the inner structures and analyzed locations.

(0.10–0.14). However, all the samples show a restricted I_{Sr} variation (0.703173–0.703983), which is slightly enriched compared to N-MORB (Fig. 12).

7. Discussion

7.1. Ages of the Tuwu–Yandong deposit belt

The geochronological data presented above, in conjunction with recently obtained zircon U–Pb ages on magmatic events and molybdenite Re-Os ages on mineralization from the Tuwu and Yandong deposits as well as previously published K–Ar data, are herein used to constrain the magmatic evolution of the Tuwu–Yandong porphyry Cu belt.

Based on the single grain zircon U–Pb data obtained from the volcanic rocks, Rui et al. (2002) suggested that 390–360 Ma might be the best estimate for the age of volcanic rocks in the Qi'eshan Group. In this study, the inherited zircon grains of about 360 Ma are found in the plagiogranite porphyry, quartz porphyry and quartz albite porphyry. These inherited zircon grains are probably captured from the surrounding rocks during the emplacement the magma. Regional mapping indicates that the Qi'eshan Group has been intruded by the plagiogranite porphyry, quartz albite porphyry and quartz porphyry. Therefore, the timing of crystallization of the inherited zircon grains may represent the age of volcanic rocks in the Qi'eshan Group. Multiple ages of the plagiogranite porphyry have been reported, including a single grain zircon U–Pb age of 361.8 ± 7.8 Ma (Rui et al., 2002), three SHRIMP zircon U–Pb dates of 334 ± 3 Ma, 333 ± 4 Ma (Chen et al., 2005), and 335.0 ± 3.7 Ma (Wang et al., 2014), and four SIMS zircon U–Pb dates of 332.2 ± 2.3 Ma, 332.8 ± 2.5 Ma (Shen et al., 2014a,b), 338.3 ± 1.4 Ma and 339.3 ± 1.3 Ma (Han et al., 2014). As mentioned above, the single grain zircon U–Pb data (361.8 ± 7.8 Ma) for the plagiogranite porphyry may represent the timing of crystallization of the inherited zircon grains. Meanwhile, we report new LA–ICP–MS zircon U–Pb ages of 339.3 ± 2.2 Ma for the plagiogranite porphyry, which is consistent with the result of Han et al. (2014). Hence, the plagiogranite porphyry formed during 340–332 Ma. Qin et al. (2002) reported a K–Ar age of 341.0 ± 4.9 Ma obtained for sericite in the phyllic alteration zone and Zhang et al. (2008) reported molybdenite Re-Os ages of 341–334 Ma which are consistent with the age of the plagiogranite porphyry, indicating that the phyllic alteration and part of mineralization may be related to the plagiogranite porphyry. The age of the quartz albite porphyry (324.1 ± 2.3 Ma) is obviously younger than the plagiogranite porphyry (339.3 ± 2.2 Ma) and consistent with most of the molybdenite ages (323 Ma; Rui et al., 2002; Zhang et al., 2010), which indicate there maybe two stages of mineralization existing in Tuwu–Yandong. This conclusion is also consistent with our observation in alteration and mineralization paragenesis: the quartz albite porphyry also suffered strong hydrothermal alteration and the mineral assemblages of chalcopyrite + chlorite + anhydrite + calcite were found in the quartz albite porphyry (Fig. 13a). The mineral assemblages of chalcopyrite + chlorite + anhydrite + calcite are developed in the main mineralization stage and overprinted the phyllic alteration in the early porphyry

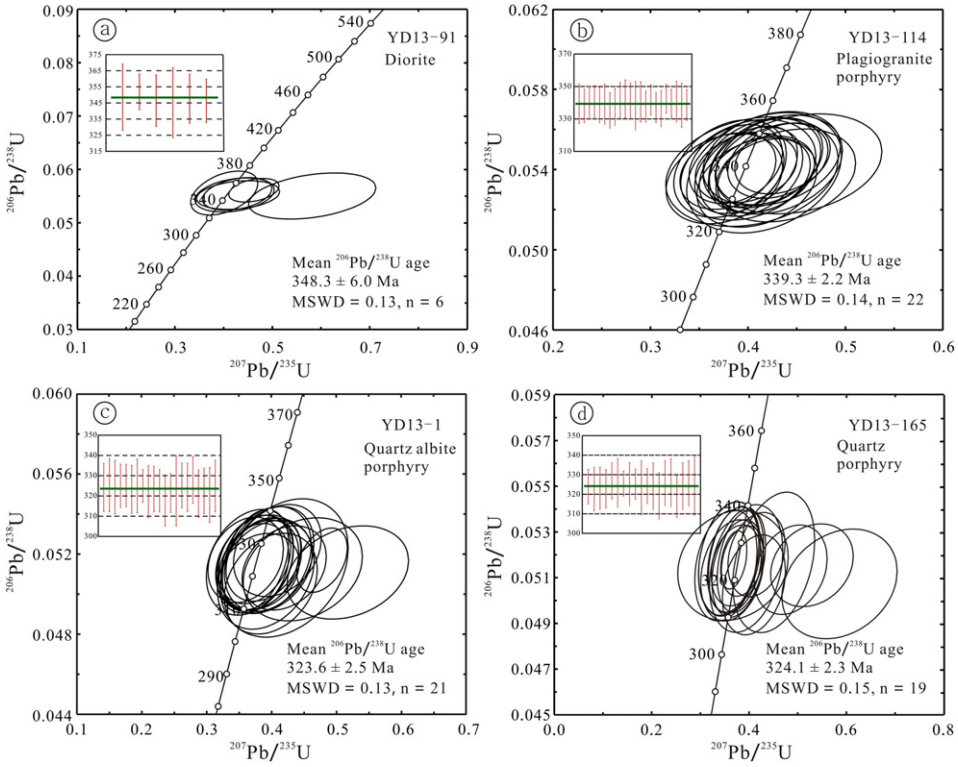

Fig. 10. $^{206}Pb/^{238}U$ versus $^{207}Pb/^{235}U$ concordia diagrams.

mineralization (Fig. 13b). In the quartz + pyrite + chalcopyrite vein of the plagiogranite porphyry (Fig. 13c), pyrites were replaced by chalcopyrite + chlorite + anhydrite + calcite (Fig. 13d). In addition, chalcopyrite intergrowth with molybdenite in the superimposed mineralization stage (Fig. 13e), suggesting that molybdenite Re-Os age (about 323 Ma) can represented the superimposed mineralization age. Furthermore, we found coarse chalcopyrite + chlorite + anhydrite + calcite in the superimposed mineralization stage cut early quartz + sericite + sulfides (Fig. 13f), which is obviously different from mineralization style of porphyry Cu deposit in the world (dominated by quartz + sulfides; Sillitoe, 2010). These evidences indicate that the quartz albite porphyry may be related to the late superimposed mineralization stage and the 323 Ma quartz albite porphyry was the late magma production postdated the 340 Ma palgiogranite.

According to the intrusive relationships, and petrographic and geochronological data, we suggested that the age sequence of magmatism in Tuwu–Yandong district is: (1) the andesite and basalt (≥360 Ma); (2) the diorite (348.3 ± 6.0 Ma); (3) the mineralized plagiogranite porphyry (340–332 Ma); (4) the quartz porphyry and quartz albite porphyry (~323 Ma). Therefore, the magmatic systems of the Tuwu–Yandong porphyry Cu belt have continued for at least ca.25 Ma.

7.2. Petrogenesis and sources of magmatism

7.2.1. The basalt, andesite and diorite

The basalts are characterized by relatively low SiO_2 (from 43.0 to 52.2 wt.%) and high Mg# (from 46 to 62), high Cr (>100 ppm) and Ni (>100 ppm), low and homogeneous $I_{Sr}(t)$ (~0.704), and high $\varepsilon_{Nd}(t)$ (+6.11 to +9.85), suggesting only limited crustal contamination was involved in their generation. This is confirmed by the lack of correlations of $I_{Sr}(t)$ with SiO_2 and MgO. Therefore, the contribution of crustal contamination in the generation of the basalts can be ignored and the geochemical and Sr–Nd isotopic compositions could be interpreted to reflect their near-primary source compositions. The basalts show fractionated LREEs and HREEs, enrichment in LREEs relative to HREEs (Fig. 6), and depletion of HFSE (Nb, Ta, Zr and Ti). In addition, they are exclusively characterized by positive $\varepsilon_{Nd}(t)$ values and low initial $I_{Sr}(t)$ ratios. In the $I_{Sr}(t)$ vs. $\varepsilon_{Nd}(t)$ diagram, the basalts plot in the OIB field, close to MORB (Fig. 12). These characters of Sr–Nd isotope suggest a juvenile source for the basalts, which is in good agreement with their young Nd model ages (T_{DM}) ranging from 0.66 to 0.52 Ga (Table 2). This is supported by the fact that no Precambrian crystalline rocks are known to occur in the Dananhu–Tousuquan belt. These trace element and Sr–Nd isotopic signatures are similar to arc magmas (Kelemen et al., 1993). In addition, in the Yb_N versus $(La/Yb)_N$ diagram, the basalts plot within normal arc andesite and dacite field (Fig. 14a). The Ancient Tianshan Ocean had subducted to the north beneath the Dananhu–Tousuquan arc before the Early Carboniferous (Xiao et al., 2004). In this scenario, the fluids and/or melts released from the subducted slab would have metasomatised the overlying supra-slab depleted asthenosphere and sub-arc lithosphere mantle sources. Therefore, the metasomatised mantle could have been the source for these basalts, which is consistent with earlier workers who have advocated a similar tectonic setting (Hou et al., 2006; Zhang et al., 2006; Shen et al., 2014a). The similar Sr–Nd isotope data, simultaneous emplacement and spatially adjacent occurrence are consistent with the basalt and andesite being related by fractional crystallization, following derivation from a homogeneous source. The basalts and andesite show a narrow La/Sm ratio range with variable La contents (Fig. 14b), suggesting that the magmas that formed the basalts underwent significant fractional crystallization (Schiano et al., 2010). The depletion of MgO, CaO, TiO_2, Fe_2O_3T, and P_2O_5 with increasing SiO_2 contents (Fig. 4) indicates fractionation of clinopyroxene, Fe-Ti oxides, and apatite, respectively. The Nb/Ta and $(Gd/Yb)_N$ ratios of the basalt and andesite range from 2.43 to 37.3 and from 1.18 to 2.27, respectively. Such high Nb/Ta ratios can only be explained by residual rutile in the subducting plate without significant amounts of residual amphibole present (König and Schuth, 2011). Low Nb/La at low Zr/Sm ratios for the basalt and andesite also

Table 1
Zircon Hf isotopic features.

	Age (Ma)	$^{176}Yb/^{177}Hf$	1σ	$^{176}Lu/^{177}Hf$	1σ	$^{176}Hf/^{177}Hf$	1σ	$\varepsilon_{Hf}(0)$	$\varepsilon_{Hf}(t)$	T_{DM1}	T_{DM2}	$f_{Lu/Hf}$
Albite quartz porphyry (sample YD13-1)												
YD13-1-1	324.2	0.054814	0.000460	0.002223	0.000021	0.282850	0.000013	2.77	9.42	589	733	−0.93
YD13-1-2	325.3	0.037213	0.000628	0.001487	0.000023	0.282908	0.000012	4.80	11.64	494	592	−0.96
YD13-1-3	359.0	0.053581	0.000327	0.002112	0.000012	0.282857	0.000013	3.02	10.42	576	696	−0.94
YD13-1-4	325.0	0.046948	0.000447	0.001785	0.000012	0.282892	0.000012	4.25	11.02	521	632	−0.95
YD13-1-5	325.2	0.057578	0.000323	0.002241	0.000015	0.282843	0.000012	2.50	9.17	600	750	−0.93
YD13-1-6	323.2	0.064536	0.000770	0.002513	0.000020	0.282877	0.000013	3.71	10.28	554	677	−0.92
YD13-1-7	323.4	0.080633	0.001109	0.003300	0.000048	0.282806	0.000014	1.20	7.61	674	849	−0.90
YD13-1-8	321.4	0.036489	0.000416	0.001473	0.000019	0.282883	0.000011	3.91	10.67	530	651	−0.96
YD13-1-9	324.2	0.069448	0.000982	0.002810	0.000039	0.282847	0.000013	2.66	9.20	603	748	−0.92
YD13-1-10	360.6	0.047262	0.000529	0.001881	0.000012	0.282896	0.000013	4.39	11.88	517	604	−0.94
YD13-1-11	324.9	0.061498	0.000595	0.002559	0.000025	0.282823	0.000012	1.81	8.41	634	799	−0.92
Plagiogranite porphyry (sample YD13-114)												
YD13-114-1	339.3	0.055317	0.000226	0.002184	0.000005	0.282877	0.000011	3.72	10.69	549	663	−0.93
YD13-114-2	338.0	0.061791	0.000718	0.002576	0.000031	0.282856	0.000013	2.96	9.82	586	718	−0.92
YD13-114-3	339.9	0.048205	0.000208	0.001970	0.000009	0.282888	0.000011	4.09	11.13	530	636	−0.94
YD13-114-4	340.7	0.034555	0.000264	0.001424	0.000012	0.282884	0.000011	3.97	11.15	527	635	−0.96
YD13-114-5	338.4	0.057729	0.000225	0.002361	0.000004	0.282885	0.000012	4.01	10.93	539	647	−0.93
YD13-114-6	338.9	0.036661	0.000737	0.001456	0.000026	0.282938	0.000010	5.86	12.99	451	516	−0.96
YD13-114-7	342.3	0.045620	0.000215	0.001882	0.000008	0.282899	0.000012	4.50	11.61	512	607	−0.94
YD13-114-8	341.0	0.034633	0.000413	0.001422	0.000017	0.282920	0.000012	5.22	12.40	477	555	−0.96
YD13-114-9	336.2	0.045169	0.000741	0.001871	0.000033	0.282849	0.000011	2.72	9.70	585	725	−0.94
YD13-114-10	364.4	0.039289	0.000187	0.001658	0.000009	0.282917	0.000012	5.11	12.74	484	552	−0.95
YD13-114-11	365.9	0.060595	0.000617	0.002474	0.000026	0.282874	0.000014	3.60	11.05	558	661	−0.93
YD13-114-12	338.4	0.043397	0.000381	0.001815	0.000020	0.282815	0.000011	1.51	8.55	633	800	−0.95
Quartz porphyry (sample YD13-165)												
YD13-165-1	323.9	0.065080	0.000413	0.002564	0.000020	0.282858	0.000009	3.03	9.61	583	721	−0.92
YD13-165-2	322.6	0.064505	0.000767	0.002475	0.000023	0.282893	0.000011	4.29	10.86	529	640	−0.93
YD13-165-3	323.1	0.041256	0.000975	0.001679	0.000043	0.282855	0.000011	2.94	9.70	573	715	−0.95
YD13-165-4	322.8	0.102302	0.002394	0.003985	0.000093	0.282827	0.000009	1.95	8.20	654	810	−0.88
YD13-165-5	326.8	0.068448	0.000617	0.002664	0.000025	0.282883	0.000010	3.92	10.54	548	664	−0.92
YD13-165-8	362.9	0.077878	0.000194	0.003012	0.000018	0.282845	0.000011	2.57	9.84	610	736	−0.91
YD13-165-9	325.0	0.060066	0.001085	0.002439	0.000044	0.282880	0.000009	3.82	10.45	548	668	−0.93
YD13-165-10	325.1	0.050692	0.000196	0.001975	0.000011	0.282872	0.000010	3.54	10.27	553	680	−0.94
YD13-165-15	325.5	0.087577	0.000829	0.003466	0.000032	0.282863	0.000012	3.21	9.63	590	721	−0.90
YD13-165-16	325.8	0.048418	0.000140	0.001910	0.000006	0.282881	0.000010	3.87	10.63	538	657	−0.94
YD13-165-19	325.5	0.096523	0.001630	0.003866	0.000067	0.282823	0.000014	1.80	8.13	658	817	−0.88

Note:
$\varepsilon_{Hf}(0) = [(^{176}Hf/^{177}Hf)_S/(^{176}Hf/^{177}Hf)_{CHUR,0} - 1] \cdot 10000$;
$\varepsilon_{Hf}(t) = \{[(^{176}Hf/^{177}Hf)_S - (^{176}Lu/^{177}Hf)_S \cdot (e^{\lambda t} - 1)]/[(^{176}Hf/^{177}Hf)_{CHUR,0} - (^{176}Lu/^{177}Hf)_{CHUR,0} \cdot (e^{\lambda t} - 1)] - 1\} \cdot 10000$;
$T_{DM1} = 1/\lambda \cdot \ln\{1 + [(^{176}Hf/^{177}Hf)_S - (^{176}Hf/^{177}Hf)_{DM}]/[(^{176}Lu/^{177}Hf)_S - (^{176}Lu/^{177}Hf)_{DM}]$;
$T_{DM2} = T_{DM1} - (T_{DM1} - t) \cdot (f_{cc} - f_s) \cdot (f_{cc} - f_{DM})$;
$f_{Lu/Hf} = [(^{176}Lu/^{177}Hf)_S/(^{176}Lu/^{177}Hf)_{CHUR,0}] - 1$;
where, $(^{176}Hf/^{177}Hf)_S$ and $(^{176}Lu/^{177}Hf)_S$ are measures values of samples, s = sample, t = crystallization time of zircon; $(^{176}Lu/^{177}Hf)_{CHUR,0} = 0.0332$ and $(^{176}Hf/^{177}Hf)_{CHUR,0} = 0.282772$ (Blichert-Toft and Albarède, 1997); $(^{176}Lu/^{177}Hf)_{DM} = 0.0384$ and $(^{176}Hf/^{177}Hf)_{DM} = 0.28325$ (Griffin et al., 2000); $f_{cc} = -0.55$ and $f_{DM} = 0.16$; $\lambda = 1.867 \times 10^{-12} yr^{-1}$ (Söderlund et al., 2004) was used in the calculation.

indicate partial melts coexist with residual rutile (Supplementary Appendix 1).

The diorite contains SiO_2 (51.0 wt.%), high MgO (5.45 wt.%) and Mg# (59), Cr (64 ppm), Ni (62 ppm), similar to those of high-Mg andesite (Tang et al., 2010), such as the high-Mg andesite in the Setouchi Volcanic Belt, Japan, which are interpreted to have been derived from partial melting of subducting lithosphere, subsequent melt-mantle interactions and equilibration with the upper-most mantle (Tatsumi, 2006). Meanwhile, the diorite has similar geochemical and mineral composition with the basalt and andesite, indicating that they have similar magma source. Thus, our favored mechanism for generating the diorite is the partial melting of mantle wedge peridotite that was previously metasomatized by slab melts, which is in accordance with the mechanism for generating the basalt and andesite.

7.2.2. The porphyries and mineralization

The plagiogranite porphyry displays chemical features suggestive of adakite affinity, characterized by relatively high Al_2O_3 (12.3–17.1 wt.%), Na_2O (3.5–4.6 wt.%), Sr (>419.6 ppm), low Y (11.3–17.2 ppm) and Yb (1.2–1.8), low Na_2O/K_2O (0.19–0.70) and markedly high Sr/Y (15.4 — 158.2). In the $I_{Sr}(t)$ vs. $\varepsilon_{Nd}(t)$ diagram (Fig. 12), the plagiogranite porphyry plots in the adakite and Archean TTG fields. It is now widely recognized that adakites or adakitic rocks may be generated by a variety of mechanisms (Castillo, 2012), such as (a) melting of subducted basaltic slab (Defant and Drummond, 1990), (b) crustal assimilation and fractional crystallization processes (AFC) of parental basaltic magmas (Castillo et al., 1999), (c) partial melting of delaminated continental lower crust (Xu et al., 2002; Wang et al., 2006), (d) partial melting of thickened lower crust (Petford and Atherton, 1996; Long et al., 2011) and (f) partial melting of subducting continental crust (Wang et al., 2008). Adakitic rocks derived by melting of lower crust are characterized by relatively low MgO or Mg# values similar to those of experimental melts from metabasalts and eclogites (Fig. 5), such as adakitic rocks in southern Tibet (Hou et al., 2004). These are not consistent with the plagiogranite porphyry from this study. The plagiogranite porphyry has low $^{87}Sr/^{86}Sr$, high $^{143}Nd/^{144}Nd$ ratios and $\varepsilon_{Hf}(t)$, similar to Cenozoic subducting oceanic crust-derived adakites, whereas adakitic rocks derived from lower crust or subducting continental crust should have higher $^{87}Sr/^{86}Sr$ and lower $^{143}Nd/^{144}Nd$ ratios, and lower $\varepsilon_{Hf}(t)$ (Wang et al., 2006; S.A. Liu et al., 2010). It is also unlikely that AFC processes

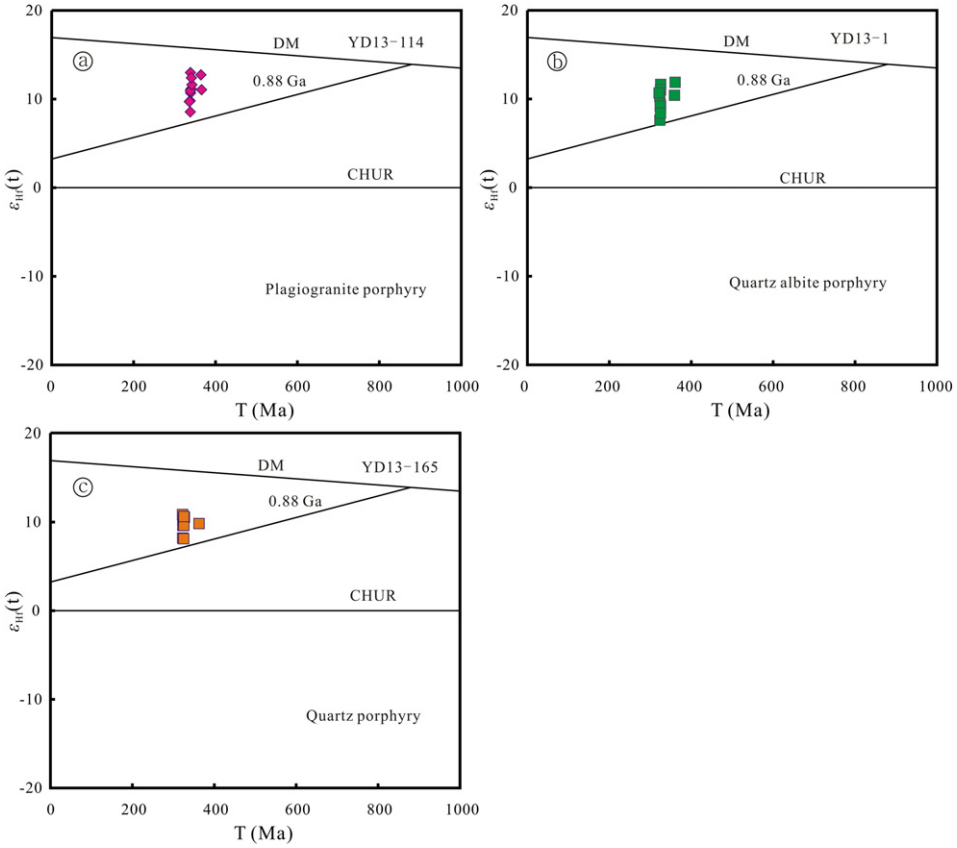

Fig. 11. Diagrams of zircon $\varepsilon_{Hf}(t)$ values vs. apparent ages of the individual zircon.

of parental basaltic magmas produced the plagiogranite porphyry. Adakitic magmas formed by AFC processes of parental basaltic magmas would show significant systematic variations in geochemistry and Sr-Nd isotopic compositions (Long et al., 2011), however, the plagiogranite porphyry rocks have uniform $\varepsilon_{Nd}(t)$, I_{Sr} and $\varepsilon_{Hf}(t)$ values, a narrow range in compositions (64.3–74.4 wt.% SiO_2) and no mafic enclaves, which are inconsistent with adakites from AFC processes of parental basaltic magmas. Furthermore, the plagiogranite porphyry samples define a straightly positive correlation line on the La vs. La/Sm diagram (Fig. 14b), implying that their compositional variations are mainly controlled by the partial melting process. Moreover, the plagiogranite porphyry falls within the subducted oceanic crust-derived adakites field (Fig. 14a). In summary, the data imply that the plagiogranite porphyry was generated by partial melting of subducted basaltic (oceanic) slab.

The plagiogranite porphyry has high $\varepsilon_{Nd}(t)$, low I_{Sr}, and K_2O, generally coincide with the oceanic slab-derived adakites, such as those from western Panama and southeastern Costa Rica (Defant et al., 1992) and Cerro Pampa (Kay et al., 1993). The plagiogranite porphyry have high Mg# and moderate to high Cr and Ni contents, consistent with the interaction of slab partial melts and peridotite during ascent through the mantle wedge. The plagiogranite porphyry has high SiO_2 (64.3–74.4 wt.%) and low MgO (<2.25 wt.%), consistent with high-SiO_2-adakites (HSAs; Martin et al., 2005), and suggesting that the plagiogranite porphyry derived from interactions between slab-derived melts and mantle peridotites. The relatively high Sr/Y ratios (Supplementary Appendix 1) of the plagiogranite porphyry are explained by the presence of garnet in the source, and zero or positive Eu anomalies are thought to be due to the absence of plagioclase in the melt residue (Tang et al., 2010). On the other hand, the plagiogranite porphyry has negative Nb, Ta and Ti anomalies, suggesting the presence of residual rutile in the source (Xiong, 2006).

The similar Sr–Nd–Hf isotopes and geochemical features with the plagiogranite porphyry indicate the quartz albite porphyry and quartz porphyry may be also derived from a juvenile material. However, compared with the plagiogranite porphyry, the quartz albite porphyry and quartz porphyry exhibit lower Mg# (Fig. 5b) and whole-rock $(La/Yb)_N$ ratios. In the SiO_2 versus Mg# diagram, the quartz albite porphyry and quartz porphyry all plot in the thick lower crust derived adakites. Compared with the plagiogranite porphyry, the zircon from the quartz albite porphyry and quartz porphyry show a wider range of δEu (0.27–0.62) which is consistent with the fractionation of plagioclase (Hoskin and Schaltegger, 2003). Therefore, the data imply that the quartz albite porphyry and quartz porphyry were generated by partial melting of juvenile lower crust.

A large number of experimental and geological studies have indicated that the magnitude of Ce^{4+}/Ce^{3+} ratio of zircon can be used as a proxy for oxygen fugacity (Ballard et al., 2002; Liang et al., 2006; Trail et al., 2011, 2012; Sun et al., 2015). Zircon grains from the ore-bearing plagiogranite porphyry have higher Ce^{4+}/Ce^{3+} ratios than zircon grains from the quartz albite porphyry and quartz porphyry. These suggest the ore-bearing plagiogranite porphyry formed from more oxidized magma, which suggests a more water-rich source for the plagiogranite porphyry than the quartz albite porphyry and quartz porphyry (Wang et al., 2013). This is consistent with the lower magmatic temperatures (as shown by Ti-in-zircon thermometry) of the ore-bearing plagiogranite porphyry. However, compared with adakitic intrusions related to porphyry Cu deposit in Chile (Figs. 8c and 14a), it is worthy of note here that the plagiogranite porphyry has lower zircon Ce^{4+}/Ce^{3+} ratios and whole-rock $(La/Yb)_N$ ratios.

Table 2
Results of whole-rock Sr–Nd isotopic analysis.

Sample	Rock type	Rb (ppm)	Sr (ppm)	$^{87}Rb/^{86}Sr$	$^{87}Sr/^{86}Sr$	I_{Sr}	Nd (ppm)	Sm (ppm)	$^{147}Sm/^{144}Nd$	$^{143}Nd/^{144}Nd$	$f_{Sm/Nd}$	T_{DM} (Ga)	$\varepsilon_{Nd}(0)$	$\varepsilon_{Nd}(t)$
TW206-1[a]	Basalt	8.11	978	0.02	0.703811 ± 14	0.703703	20.1	4.29	0.13	0.512855 ± 13	−0.34	0.53	4.23	7.17
TW206-2[a]	Basalt	3.10	709	0.01	0.704022 ± 18	0.703965	21.0	4.90	0.14	0.512861 ± 13	−0.28	0.61	4.35	6.76
Bb-158[b]	Basalt			0.08	0.704122	0.703771			0.14	0.512828	−0.29	0.66	3.71	6.21
Bb-162[b]	Basalt			0.01	0.703679	0.703647			0.13	0.512854	−0.35	0.52	4.21	7.22
Bb-270[b]	Basalt			0.01	0.703921	0.703881			0.11	0.512769	−0.42	0.59	2.56	6.11
Bb-185[b]	Andesite			0.05	0.704031	0.703794			0.15	0.512861	−0.24	0.68	4.35	6.41
TW201[a]	Andesite	4.20	707	0.02	0.703713 ± 13	0.703636	16.6	4.21	0.15	0.512859 ± 12	−0.22	0.74	4.31	6.20
R-01[a]	Plagiogranite porphyry	20	624	0.09	0.703877 ± 12	0.703459			0.12	0.512944	−0.37	0.35	5.97	9.16
R-02[a]	Plagiogranite porphyry	19	391	0.14	0.704099 ± 11	0.703465			0.11	0.512806	−0.43	0.52	3.28	6.94
R-03[a]	Plagiogranite porphyry	26	457	0.16	0.703955 ± 14	0.703219			0.11	0.512812	−0.43	0.51	3.39	7.08
R-04[a]	Plagiogranite porphyry	20	327	0.18	0.704175 ± 13	0.703374			0.12	0.512870	−0.40	0.44	4.53	7.97
R-06[a]	Plagiogranite porphyry	58	452	0.37	0.704975 ± 11	0.703306			0.10	0.512767	−0.49	0.52	2.52	6.67
R-07[a]	Plagiogranite porphyry	65	293	0.63	0.706739 ± 24	0.703853			0.10	0.512730	−0.47	0.58	1.79	5.83
YD203[a]	Plagiogranite porphyry	20	473	0.12	0.704377 ± 17	0.703830	11.3	2.51	0.13	0.512757 ± 13	−0.32	0.76	2.32	5.02
TW208[a]	Plagiogranite porphyry	40	630	0.18	0.704286 ± 11	0.703466	9.8	1.77	0.11	0.512744 ± 9	−0.44	0.59	2.07	5.87
TW203[a]	Plagiogranite porphyry	31	321	0.27	0.704783 ± 10	0.703531	6.2	1.12	0.11	0.512773 ± 11	−0.44	0.55	2.63	6.43
TW204[a]	Plagiogranite porphyry	38	552	0.19	0.704250 ± 12	0.703363	11.6	2.43	0.13	0.512824 ± 12	−0.35	0.58	3.63	6.64
TW219[a]	Plagiogranite porphyry	19	679	0.08	0.703898 ± 13	0.703534	19.9	4.16	0.13	0.512872 ± 11	−0.36	0.49	4.56	7.62
YD13-114-1	Plagiogranite porphyry	51	140	1.05	0.709044 ± 8	0.704281	6.7	1.42	0.13	0.512809 ± 5	−0.35	0.61	3.33	6.31
YD13-1-1	Quartz albite porphyry	28	853	0.09	0.704120 ± 7	0.703693	13.1	2.92	0.13	0.512786 ± 3	−0.31	0.70	2.89	5.42
YD13-143	Quartz albite porphyry	39	739	0.15	0.704258 ± 7	0.703567	13.5	3.04	0.14	0.512771 ± 4	−0.31	0.75	2.59	5.07

Data marked by [a] and [b] are derived from Zhang et al. (2006) and Xia et al. (2004), respectively.

7.3. Implications on tectonic setting

Carboniferous magmatic rocks are widely exposed in the Tuwu–Yandong deposit area (Qin et al., 2002; Rui et al., 2002; Xia et al., 2004; Xiao et al., 2004; Han et al., 2006; Wang et al., 2006; Han et al., 2014; Shen et al., 2014a; Wang et al., 2014) and these rocks have been suggested to have formed in a variety of different tectonic settings. Xia et al. (2004) proposed out that in the Carboniferous, the Paleozoic ocean basin, which is now the Tianshan area had already closed and the Tianshan orogenic belt entered a post-orogenic rift (extensional) stage. According to this model, the Carboniferous magmatic rocks in the Tuwu–Yandong deposit area were formed in a continental rift environment (Xia et al., 2008). However, during the Devonian to Early Carboniferous, N-dipping subduction of the ancient Tianshan Ocean occurred beneath the Dananhu–Tousuquan arc, giving rise to the Kanggurtag forearc basin/accretionary complex. The rhyolitic porphyry and mylonitic andesites in the Kanggurtag and Shiyingtan gold mines formed between 299 and 285 Ma, indicating that the Kanggurtag accretionary process may have lasted to the Early Permian (Xiao et al., 2004).

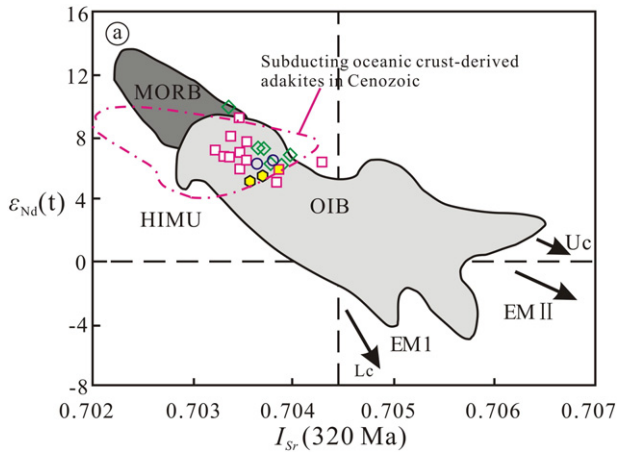

Fig. 12. I_{Sr} versus $\varepsilon_{Nd}(t)$ diagram. Legends same as for Fig. 3. The data for the Subducting oceanic crust-derived adakites in Cenozoic are from Wang et al. (2006).

In addition, Wang et al. (2002) reported isotopic ages of 276–254 Ma for large-scale ductile shear zones in the Kanggurtag area which they thought were post-subduction structures. Thus, Xiao et al. (2004) concluded that subduction ceased in the Early Permian as a result of collision of the Dananhu–Tousuquan arc and the Middle Tianshan massif. Most geologists argue that the Carboniferous magmatic rocks in the Tuwu–Yandong deposit area were related to the subduction tectonic setting (Xiao et al., 2004; Hou et al., 2006; Zhang et al., 2006; Xiao et al., 2009; Qin et al., 2011; Han et al., 2014; Shen et al., 2014b; Wang et al., 2014). The Carboniferous period is the main stage for the formation of arc-related porphyry Cu and epithermal Au and basin-related VMS (volcanic massive sulfide) deposits in Tianshan and circum-Junggar area (Qin et al., 2011). In this study, the geochronological and geochemical evidence indicates that the subduction of an oceanic slab may have been responsible for the generation of the basalt and andesite, adakitic rocks (the plagiogranite porphyry), high-Mg diorite, quartz albite porphyry and quartz porphyry in the Tuwu–Yandong deposit area (Tang et al., 2010), similar to modern rock associations in Japan (Tatsumi, 2006), which is not consistent with the rift model proposed by Xia et al. (2004) and Xia et al. (2008).

As discussed above, the plagiogranite porphyry is derived from the partial melting of the ancient Tianshan oceanic slab. Numerical and petrological studies of pressure-temperature-time (PTT) paths in subduction zones suggest that partial melting of the subducted slab generally occurs only with very young (≤5 Ma) lithosphere (Peacock et al., 1994). Song et al. (2002) have reported an age based on zircon U–Pb SHRIMP data of 358 ± 7 Ma for a granodiorite and 383 ± 9 Ma for a monzogranite in the Dananhu–Tousuquan arc, which are interpreted to be related to the subduction tectonic setting. This indicates that the subduction of the ancient Tianshan Ocean started in the Middle Devonian (Xiao et al., 2004; Han et al., 2014) and the plagiogranite porphyry with adakitic features formed at least 40 m.y. later. Past research has shown that flat subduction can produce the temperature and pressure conditions necessary for fusion of moderately old oceanic crust (Gutscher et al., 2000; Li and Li, 2007). Hence, we propose a flat subduction that started ca. 340 Ma and resulted in formation of the adakitic plagiogranite porphyry after a period of "steady" subduction responsible for the basalt and andesite (Fig. 15a and b). Flattening of the subducting slab could not only tectonically thicken the crust but also squeeze out the mantle wedge, and thus terminate the arc magmatism in the volcanic front region with adakites being generated as the ending phase (Wen et al., 2008). Gradual flattening of

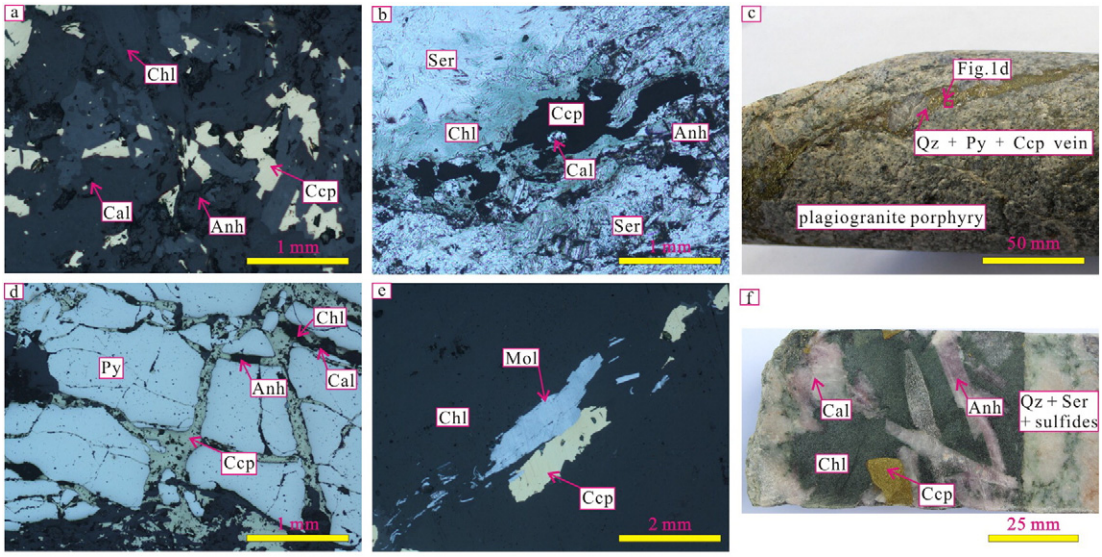

Fig. 13. Photomicrographs showing: (a) chalcopyrite + chlorite + anhydrite + calcite in the quartz albite porphyry; (b) chalcopyrite + chlorite + anhydrite + calcite intersect the phyllic alteration in the early porphyry mineralization; (c) a quartz + pyrite + chalcopyrite vein in the plagiogranite porphyry; (d) pyrite replaced by chalcopyrite + chlorite + anhydrite + calcite in the plagiogranite porphyry; (e) chalcopyrite + chlorite + molybdenite in the superimposed mineralization stage; (f) coarse chalcopyrite + chlorite + anhydrite + calcite in the superimposed mineralization stage intersect quartz + sericite + sulfides. Anh = anhydrite, Cal = calcite, Ccp = chalcopyrite, Chl = chlorite, Mol = molybdenite, Py = pyrite, Qz = quartz, Ser = sericite.

the ancient Tianshan Ocean beneath the Dananhu arc could explain the LILE and LREE enrichment recorded in the magma of the Tuwu–Yandong deposit as this would result in squeezing out of the sub-arc mantle and reduced circulation in the wedge. This also leaded to the generation of oxidized melts that can transport copper, gold, and sulfur dioxide from the mantle. As a result of flat subduction, large cumulative volumes of hydrous fluids derived by dehydration of the downgoing slab may have percolated through the non-convecting wedge rather than being stripped out by the continuous replenishment of the asthenosphere (Hollings et al., 2011). Flat subduction occurs as oceanic plateau, seamount or ridge being subducted. However, further studies are needed to confirm this issue in the Tuwu–Yandong district. After flat subduction, the rollback of the subducted slab caused strong upwelling of the asthenosphere, provoking strong asthenosphere–lithosphere interaction and partial melting of juvenile lower crust (Fig. 15c). The slab rollback model is compatible with that the quartz albite porphyry and quartz porphyry have lower zircon Ce^{4+}/Ce^{3+} ratios than the plagiogranite porphyry (Li et al., 2012). No younger magmatism have been identified after 323 Ma in the Tuwu–Yandong district, which may indicate a “quiet period” before final collision along the Kangguer Fault in this area.

8. Conclusions

(1) The Tuwu–Yandong porphyry Cu belt is located in the East Tianshan mountains, in the eastern Central Asian Orogenic Belt. The LA–ICP–MS zircon U–Pb isotopic analyses reveal that the age sequence of magmatism in Tuwu–Yandong district is: (1) the andesite and basalt (≥360 Ma); (2) the diorite (348.3 ± 6.0 Ma); (3) the mineralized plagiogranite porphyry (340–332 Ma); (4) the quartz porphyry and quartz albite porphyry (~323 Ma).

(2) Whole-rock elemental and Sr–Nd–Hf isotope data, in conjunction with mineral compositions suggest that the parental magma of the basalt, andesite and diorite is interpreted to have been derived from partial melting of mantle-wedge peridotite, while the plagiogranites have been derived by a partial melting of the subducted oceanic crust followed by adakitic melt-mantle peridotite interaction. The quartz albite and quartz porphyry are characterized by similar Sr–Nd–Hf isotope but lower Mg# and whole-rock $(La/Yb)_N$ ratios to the plagiogranite porphyry, suggesting they were derived from juvenile lower crust, and negative Eu anomalies suggest fractionation of plagioclase.

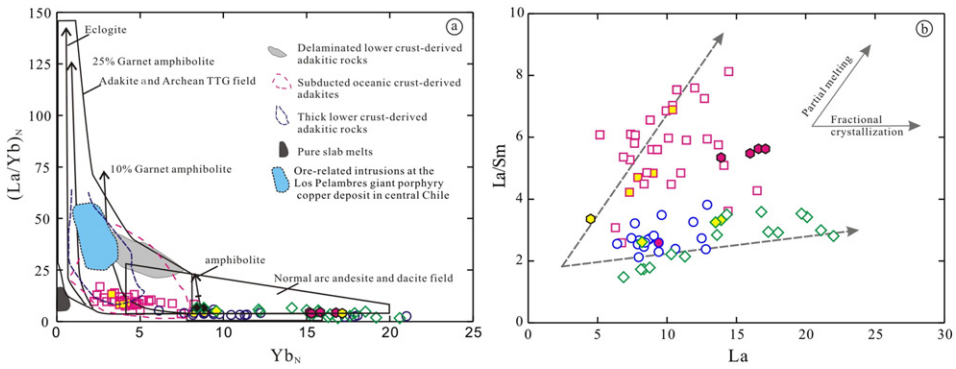

Fig. 14. (a) La/Sm versus La diagram. (b) $(La/Yb)_N$ versus Yb_N diagram, after Wang et al. (2006). Legends same as for Fig. 3. The data for Ore-related intrusions at the Los Pelambres giant porphyry copper deposit in central Chile are from Reich et al. (2003).

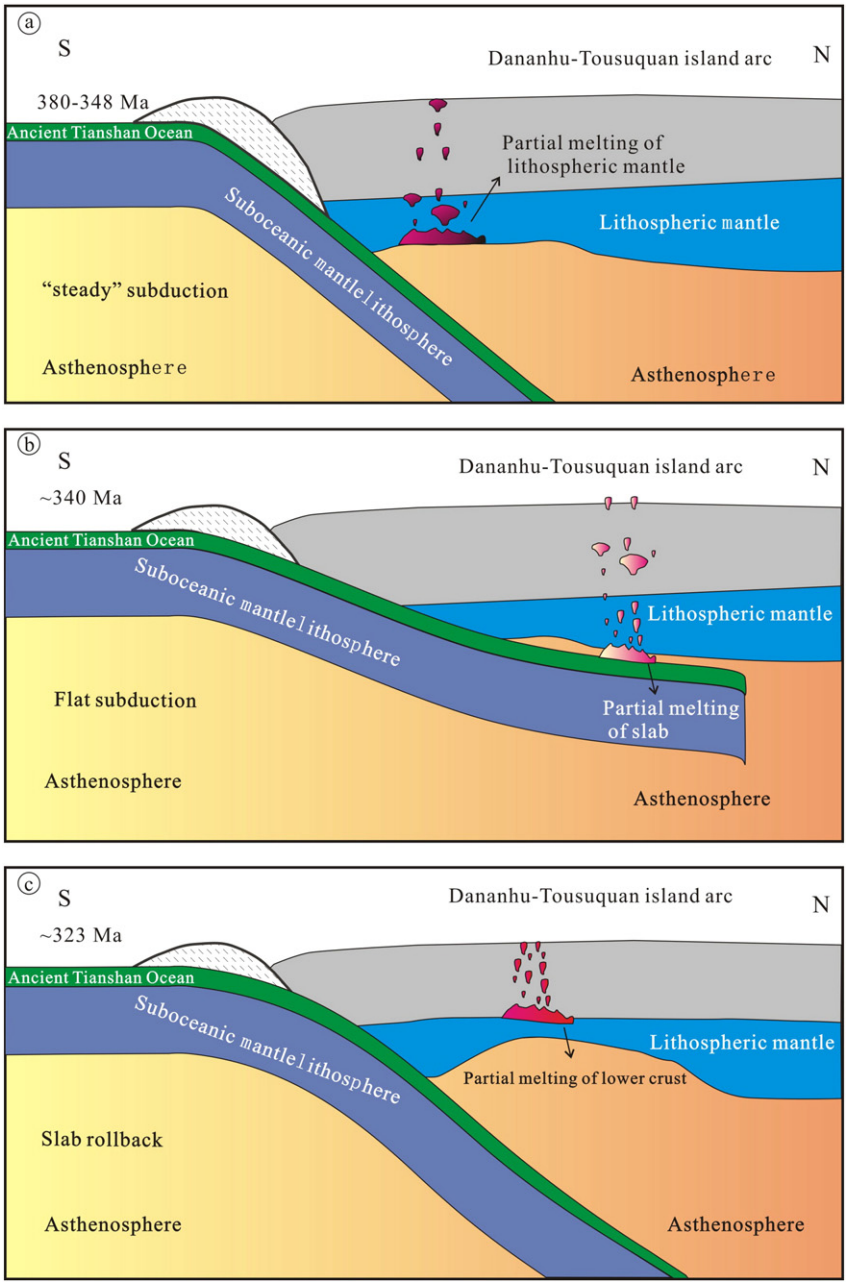

Fig. 15. Illustrations of (a) the proposed tectonic context for the development of volcanic rocks in the Tuwu and Yandong deposits, induced by "steady" subduction of the Ancient Tianshan Ocean (b) partial melting of subducted slab, and subsequent melt–mantle interaction, producing the plagiogranite porphyry, induced by flat subduction, and (c) partial melting of lower crust, induced by slab rollback.

(3) A flat subduction that started ca. 340 Ma and resulted in formation of the adakitic plagiogranite porphyry after a period of "steady" subduction, experienced slab rollback at around 323 Ma.

Supplementary data to this article can be found online at http://dx.doi.org/10.1016/j.gr.2015.09.003.

Acknowledgments

This study was financially supported by the Chinese National 973-program (Project 2014CB440802 and 2014CB448000). We are grateful to a number of technical staff for assistance during this study, especially Wu Lei for assistance during zircon CL imaging; Ma Jinlong for assistance during whole-rock Sr-Nd analysis; and Li Congying and Tu Xianglin for assistance during zircon LA–ICP–MS U–Pb–Hf analysis. We also thank Zhao Guochun for editorial handling and two anonymous reviewers for their constructive comments, which significantly improved the manuscript. This is contribution No. IS-2126 from GIGCAS.

References

Allen, M.B., Windley, B.F., Zhang, C., 1993. Palaeozoic collisional tectonics and magmatism of the Chinese Tien Shan, central Asia. Tectonophysics 220, 89–115.

Ballard, J.R., Palin, M.J., Campbell, I.H., 2002. Relative oxidation states of magmas inferred from Ce(IV)/Ce(III) in zircon: application to porphyry copper deposits of northern Chile. Contributions to Mineralogy and Petrology 144, 347–364.

Blichert-Toft, J., Albarède, F., 1997. The Lu–Hf isotope geochemistry of chondrites and the evolution of the mantle–crust system. Earth and Planetary Science Letters 148, 243–258.

Castillo, P.R., 2012. Adakite petrogenesis. Lithos 134–135, 304–316.

Castillo, P.R., Janney, P.E., Solidum, R.U., 1999. Petrology and geochemistry of Camiguin Island, southern Philippines: insights to the source of adakites and other lavas in a complex arc setting. Contributions to Mineralogy and Petrology 134, 33–51.
Chen, F.W., Li, H.Q., Chen, Y.C., Wang, D.H., Wang, J.L., Liu, D.Q., Tang, Y.L., Zhou, R.H., 2005. Zircon SHRIMP U–Pb dating and its geological significance of mineralization in Tuwu–Yandong porphyry copper mine, east Tianshan mountain. Acta Geologica Sinica 79, 256–261 (in Chinese with English abstract).
Chen, H.Y., Chen, Y.J., Baker, M.J., 2012a. Evolution of ore-forming fluids in the Sawayaerdun gold deposit in the Southwestern Chinese Tianshan metallogenic belt, Northwest China. Journal of Asian Earth Sciences 49, 131–144.
Chen, H.Y., Yang, J.T., Baker, M., 2012b. Mineralization and fluid evolution of the Jiyuan polymetallic Cu–Ag–Pb–Zn–Au deposit, eastern Tianshan, NW China. International Geology Review 54, 816–832.
Defant, M.J., Drummond, M.S., 1990. Derivation of some modern arc magmas by melting of young subducted lithosphere. Nature 347, 662–665.
Defant, M.J., Jackson, T.E., Drummond, M.S., De Boer, J.Z., Bellon, H., Feigenson, M.D., Maury, R.C., Stewart, R.H., 1992. The geochemistry of young volcanism throughout western Panama and southeastern Costa Rica: an overview. Journal of the Geological Society 149, 569–579.
Ferry, J.M., Watson, E.B., 2007. New thermodynamic models and revised calibrations for the Ti-in-zircon and Zr-in-rutile thermometers. Contributions to Mineralogy and Petrology 154, 429–437.
Gao, J., Li, M.S., Xiao, X.C., Tang, Y.Q., He, G.Q., 1998. Paleozoic tectonic evolution of the Tianshan Orogen, northwestern China. Tectonophysics 287, 213–231.
Gao, J., Long, L.L., Klemd, R., Qian, Q., Liu, D.Y., Xiong, X.M., Su, W., Liu, W., Wang, Y.T., Yang, F.Q., 2009. Tectonic evolution of the South Tianshan orogen and adjacent regions, NW China: geochemical and age constraints of granitoid rocks. International Journal of Earth Sciences 98, 1221–1238.
Griffin, W.L., Pearson, N.J., Belousova, E., Jackson, S.E., Van Achterbergh, E., O'Reilly, S.Y., Shee, S.R., 2000. The Hf isotope composition of cratonic mantle: LA–MC–ICPMS analysis of zircon megacrysts in kimberlites. Geochimica et Cosmochimica Acta 64, 133–147.
Guo, R.R., Liu, S.W., Santosh, M., Li, Q.G., Bai, X., Wang, W., 2013. Geochemistry, zircon U–Pb geochronology and Lu–Hf isotopes of metavolcanics from eastern Hebei reveal Neoarchean subduction tectonics in the North China Craton. Gondwana Research 24, 664–686.
Gutscher, M.A., Maury, R., Eissen, J.P., Bourdon, E., 2000. Can slab melting be caused by flat subduction? Geology 28, 535–538.
Han, C.M., Xiao, W.J., Zhao, G.C., Mao, J.W., Yang, J.M., Wang, Z.L., Yan, Z., Mao, Q.G., 2006. Geological characteristics and genesis of the Tuwu porphyry copper deposit, Hami, Xinjiang, Central Asia. Ore Geology Reviews 29, 77–94.
Han, Z.K., Han, C.M., Xiao, W.J., Zhao, G.C., Wang, Z.M., Ao, S.J., Zhang, J., Wan, B., 2014. Palaeozoic porphyry Cu–Au and ultramafic Cu–Ni deposits in the eastern Tianshan orogenic belt: temporal constraints from U–Pb geochronology. International Geology Review 55, 842–862.
Hollings, P., Wolfe, R., Cooke, D.R., Waters, P.J., 2011. Geochemistry of tertiary igneous rocks of Northern Luzon, Philippines: evidence for a back-arc setting for alkalic porphyry copper–gold deposits and a case for slab roll-back? Economic Geology 106, 1257–1277.
Hoskin, P.W.O., Schaltegger, U., 2003. The composition of zircon and igneous and metamorphic petrogenesis. Reviews in Mineralogy and Geochemistry 53, 27–62.
Hou, Z.Q., Gao, Y.F., Qu, X.M., Rui, Z.Y., Mo, X.X., 2004. Origin of adakitic intrusives generated during mid-Miocene east–west extension in southern Tibet. Earth and Planetary Science Letters 220, 139–155.
Hou, G.S., Tang, H.F., Liu, C.Q., Wang, Y.B., 2005. Geochronological and geochemical study on the wallrock of Tuwu–Yandong porphyry copper deposits, eastern Tianshan mountains. Acta Petrologica Sinica 21, 1729–1736 (in Chinese with English abstract).
Hou, G.S., Tang, H.F., Liu, C.Q., 2006. Geochemical characteristics of the Late Paleozoic Volcanics in Jueluotage tectonic belt, eastern Tianshan and its implications. Acta Petrologica Sinica 22, 1167–1177 (in Chinese with English abstract).
Hou, T., Zhang, Z.C., Santosh, M., Encarnacion, J., Zhu, J., Luo, W.J., 2014. Geochronology and geochemistry of submarine volcanic rocks in the Yamansu iron deposit, Eastern Tianshan Mountains, NW China: constraints on the metallogenesis. Ore Geology Reviews 56, 487–502.
Kay, S.M., Ramos, V.A., Marquez, M., 1993. Evidence in Cerro Pampa volcanic rocks for slab-melting prior to ridge-trench collision in southern South America. The Journal of Geology 703–714.
Kelemen, P.B., Shimizu, N., Dunn, T., 1993. Relative depletion of niobium in some arc magmas and the continental crust: partitioning of K, Nb, La and Ce during melt/rock reaction in the upper mantle. Earth and Planetary Science Letters 120, 111–134.
König, S., Schuth, S., 2011. Deep melting of old subducted oceanic crust recorded by superchondritic Nb/Ta in modern island arc lavas. Earth and Planetary Science Letters 301, 265–274.
Li, Z.X., Li, X.H., 2007. Formation of the 1300-km-wide intracontinental orogen and postorogenic magmatic province in Mesozoic South China: a flat-slab subduction model. Geology 35, 179–182.
Li, Q.G., Liu, S.W., Han, B.F., Zhang, J., Chu, Z.Y., 2005. Geochemistry of metasedimentary rocks of the Proterozoic Xingxingxia complex: implications for provenance and tectonic setting of the eastern segment of the Central Tianshan Tectonic Zone, northwestern China. Canadian Journal of Earth Sciences 42, 287–306.
Li, X.M., Xia, L.Q., Xia, Z.C., Xue, X.Y., Ma, Z.P., Wang, L.S., 2006. Petroginesis of the Carboniferous Qi'eshan group volcanic rocks in the East Tianshan. Journal of Jilin University (Earth Science Edition) 36, 336–341 (in Chinese with English abstract).
Li, X.H., Long, W.G., Li, Q.L., Liu, Y., Zheng, Y.F., Yang, Y.H., Chamberlain, K.R., Wan, D.F., Guo, C.H., Wang, X.C., Tao, H., 2010. Penglai zircon megacrysts: a potential new working reference material for microbeam determination of Hf–O isotopes and U–Pb age. Geostandards and Geoanalytical Research 34, 117–134.
Li, C.Y., Zhang, H., Wang, F.Y., Liu, J.Q., Sun, Y.L., Hao, X.L., Li, Y.L., Sun, W.D., 2012. The formation of the Dabaoshan porphyry molybdenum deposit induced by slab rollback. Lithos 150, 101–110.
Li, X.H., Tang, G.Q., Gong, B., Yang, Y.H., Hou, K.J., Hu, Z.C., Li, Q.L., Liu, Y., Li, W.X., 2013. Qinghu zircon: a working reference for microbeam analysis of U–Pb age and Hf and O isotopes. Chinese Science Bulletin 58, 4647–4654.
Liang, H.Y., Campbell, I.H., Allen, C., Sun, W.D., Liu, C.Q., Yu, H.X., Xie, Y.W., Zhang, Y.Q., 2006. Zircon Ce^{4+}/Ce^{3+} ratios and ages for Yulong ore-bearing porphyries in eastern Tibet. Mineralium Deposita 41, 152–159.
Liu, S.A., Li, S.G., He, Y.S., Huang, F., 2010. Geochemical contrasts between early Cretaceous ore-bearing and ore-barren high-Mg adakites in central-eastern China: implications for petrogenesis and Cu–Au mineralization. Geochimica et Cosmochimica Acta 74, 7160–7178.
Liu, Y.S., Hu, Z.C., Zong, K.Q., Gao, C.G., Gao, S., Xu, J., Chen, H.H., 2010. Reappraisement and refinement of zircon U–Pb isotope and trace element analyses by LA–ICP–MS. Chinese Science Bulletin 55, 1535–1546.
Liu, S.W., Zhang, J., Li, Q.G., Zhang, L.F., Wang, W., Yang, P.T., 2012. Geochemistry and U–Pb zircon ages of metamorphic volcanic rocks of the Paleoproterozoic Lüliang Complex and constraints on the evolution of the Trans-North China Orogen, North China Craton. Precambrian Research 222–223, 173–190.
Long, X.P., Yuan, C., Sun, M., Kröner, A., Zhao, G.C., Wilde, S., Hu, A., 2011. Reworking of the Tarim Craton by underplating of mantle plume-derived magmas: evidence from Neoproterozoic granitoids in the Kuluketage area, NW China. Precambrian Research 187, 1–14.
Ludwig, K.R., 2003. Isoplot/Ex, Version 3: A Geochronological Toolkit For Microsoft Excel. Geochronology Center Berkeley, Berkeley, California.
Ma, R.S., Shu, L.S., Sun, J.Q., 1997. Tectonic Evolution And Metallogeny Of Eastern Tianshan Mountains. Geological Publishing House (in Chinese).
Mao, J.W., Pirajno, F., Zhang, Z.H., Chai, F.M., Wu, H., Chen, S.P., Cheng, L.S., Yang, J.M., Zhang, C.Q., 2008. A review of the Cu–Ni sulphide deposits in the Chinese Tianshan and Altay orogens (Xinjiang Autonomous Region, NW China): principal characteristics and ore-forming processes. Journal of Asian Earth Sciences 32, 184–203.
Martin, H., Smithies, R.H., Rapp, R., Moyen, J.F., Champion, D., 2005. An overview of adakite, tonalite–trondhjemite–granodiorite (TTG), and sanukitoid: relationships and some implications for crustal evolution. Lithos 79, 1–24.
Muñoz, M., Charrier, R., Fanning, C., Maksaev, V., Deckart, K., 2012. Zircon trace element and O–Hf Isotope analyses of mineralized intrusions from El Teniente ore deposit, Chilean Andes: constraints on the source and magmatic evolution of porphyry Cu–Mo related magmas. Journal of Petrology 53, 1091–1122.
Peacock, S.M., Rushmer, T., Thompson, A.B., 1994. Partial melting of subducting oceanic crust. Earth and Planetary Science Letters 121, 227–244.
Petford, N., Atherton, M., 1996. Na-rich partial melts from newly underplated basaltic crust: the Cordillera Blanca Batholith, Peru. Journal of Petrology 37, 1491–1521.
Polat, A., Hofmann, A.W., Rosing, M.T., 2002. Boninite-like volcanic rocks in the 3.7–3.8 Ga Isua greenstone belt, West Greenland: geochemical evidence for intra-oceanic subduction zone processes in the early Earth. Chemical Geology 184, 231–254.
Qin, K.Z., Sun, S., Li, J.L., Fang, T.H., Wang, S.L., Liu, W., 2002. Paleozoic epithermal Au and porphyry Cu deposits in North Xinjiang, China: epochs, features, tectonic linkage and exploration significance. Resource Geology 52, 291–300.
Qin, K.Z., Su, B.X., Sakyi, P.A., Tang, D.M., Li, X.H., Sun, H., Xiao, Q.H., Liu, P.P., 2011. SIMS zircon U–Pb geochronology and Sr–Nd isotopes of Ni–Cu-bearing mafic–ultramafic intrusions in Eastern Tianshan and Beishan in correlation with flood basalts in Tarim Basin (NW China): constraints on a ca. 280 Ma mantle plume. American Journal of Science 311, 237–260.
Reich, M., Parada, M.A., Palacios, C., Dietrich, A., Schultz, F., Lehmann, B., 2003. Adakite-like signature of Late Miocene intrusions at the Los Pelambres giant porphyry copper deposit in the Andes of central Chile: metallogenic implications. Mineralium Deposita 38, 876–885.
Rui, Z.Y., Wang, L.S., Wang, Y.T., Liu, Y.L., 2002. Discussion on metallogenic epoch of Tuwu and Yandong porphyry copper deposits in eastern Tianshan Mountains, Xinjiang. Mineral Deposits 21, 16–22 (in Chinese with English abstract).
Schiano, P., Monzier, M., Eissen, J.P., Martin, H., Koga, K.T., 2010. Simple mixing as the major control of the evolution of volcanic suites in the Ecuadorian Andes. Contributions to Mineralogy and Petrology 160, 297–312.
Shen, P., Pan, H.D., Dong, L.H., 2014a. Yandong porphyry Cu deposit, Xinjiang, China—geology, geochemistry and SIMS U–Pb zircon geochronology of host porphyries and associated alteration and mineralization. Journal of Asian Earth Sciences 80, 197–217.
Shen, P., Pan, H.D., Zhou, T.F., Wang, J.B., 2014b. Petrography, geochemistry and geochronology of the host porphyries and associated alteration at the Tuwu Cu deposit, NW China: a case for increased depositional efficiency by reaction with mafic hostrock? Mineralium Deposita 49, 709–731.
Shu, L.S., Yu, J.H., Charvet, J., Laurent-Charvet, S., Sang, H.Q., Zhang, R.G., 2004. Geological, geochronological and geochemical features of granulites in the Eastern Tianshan, NW China. Journal of Asian Earth Sciences 24, 25–41.
Sillitoe, R.H., 2010. Porphyry copper systems. Economic Geology 105, 3–41.
Söderlund, U., Patchett, P.J., Vervoort, J.D., Isachsen, C.E., 2004. The ^{176}Lu decay constant determined by Lu-Hf and U–Pb isotope systematics of Precambrian mafic intrusions. Earth and Planetary Science Letters 219, 311–324.
Song, B., Li, J.Y., Li, W.Q., Wang, K.Z., Wang, Y., 2002. SHRIMP dating of zircon from Dananhu and Keziekalasai granitoid batholith in southern margin of Tuiha basin, East Tishan, NW China and their geological implication. Xinjiang Geology 20, 342–345 (in Chinese with English abstract).

Su, B.X., Qin, K.Z., Sakyi, P.A., Li, X.H., Yang, Y.H., Sun, H., Tang, D.M., Liu, P.P., Xiao, Q.H., Malaviarachchi, S.P., 2011. U–Pb ages and Hf–O isotopes of zircons from Late Paleozoic mafic–ultramafic units in the southern Central Asian Orogenic Belt: tectonic implications and evidence for an Early–Permian mantle plume. Gondwana Research 20, 516–531.

Sun, S.S., McDonough, W.F., 1989. Chemical and isotopic systematics of oceanic basalts: implications for mantle composition and processes. In: Saunders, A.D., Norry, M.J. (Eds.), Magmatism in the ocean basin. Geological Society, London, Special Publications 42, pp. 313–345.

Sun, W.D., Huang, R.F., Li, H., Hu, Y.B., Zhang, C.C., Sun, S.J., Zhang, L.P., Ding, X., Li, C.Y., Zartman, R.E., Ling, M.X., 2015. Porphyry deposits and oxidized magmas. Ore Geology Reviews 65 (Part 1), 97–131.

Tang, G.J., Wang, Q., Wyman, D.A., Li, Z.X., Zhao, Z.H., Jia, X.H., Jiang, Z.Q., 2010. Ridge subduction and crustal growth in the Central Asian Orogenic Belt: evidence from Late Carboniferous adakites and high-Mg diorites in the western Junggar region, northern Xinjiang (west China). Chemical Geology 277, 281–300.

Tang, G.J., Wang, Q., Wyman, D.A., Li, Z.X., Zhao, Z.H., Yang, Y.H., 2012. Late carboniferous high εNd(t)–εHf(t) granitoids, enclaves and dikes in western Junggar, NW China: ridge-subduction-related magmatism and crustal growth. Lithos 140–141, 86–102.

Tatsumi, Y., 2006. High-Mg andesites in the Setouchi volcanic belt, southwestern Japan: analogy to Archean magmatism and continental crust formation? Annual Review of Earth and Planetary Sciences 34, 467–499.

Trail, D., Watson, E.B., Tailby, N.D., 2011. The oxidation state of Hadean magmas and implications for early Earth's atmosphere. Nature 480, 79–82.

Trail, D., Bruce Watson, E., Tailby, N.D., 2012. Ce and Eu anomalies in zircon as proxies for the oxidation state of magmas. Geochimica et Cosmochimica Acta 97, 70–87.

Wang, Y., Li, J.Y., Li, W.Q., 2002. $^{40}Ar/^{39}Ar$ chronological evidence of dextral shear and tectonic evolution of the eastern Tianshan orogenic belt. Xinjiang Geology 20, 315–319 (in Chinese with English abstract).

Wang, Q., Xu, J.F., Jian, P., Bao, Z.W., Zhao, Z.h., Li, C.F., Xiong, X.L., Ma, J.L., 2006. Petrogenesis of adakitic porphyries in an extensional tectonic setting, Dexing, South China: implications for the genesis of porphyry copper mineralization. Journal of Petrology 47, 119–144.

Wang, Q., Wyman, D.A., Xu, J.F., Dong, Y.H., Vasconcelos, P.M., Pearson, N., Wan, Y.S., Dong, H., Li, C.F., Yu, Y.S., Zhu, T.X., Feng, X.T., Zhang, Q.Y., Zi, F., Chu, Z.Y., 2008. Eocene melting of subducting continental crust and early uplifting of central Tibet: evidence from central-western Qiangtang high-K calc-alkaline andesites, dacites and rhyolites. Earth and Planetary Science Letters 272, 158–171.

Wang, F.Y., Liu, S.A., Li, S.G., He, Y.S., 2013. Contrasting zircon Hf–O isotopes and trace elements between ore-bearing and ore-barren adakitic rocks in central-eastern China: implications for genetic relation to Cu–Au mineralization. Lithos 156–159, 97–111.

Wang, Y.H., Xue, C.J., Wang, J.P., Peng, R.M., Yang, J.T., Zhang, F.F., Zhao, Z.N., Zhao, Y.J., 2014. Petrogenesis of magmatism in the Yandong region of Eastern Tianshan, Xinjiang: geochemical, geochronological, and Hf isotope constraints. International Geology Review http://dx.doi.org/10.1080/00206814.00202014.00900653.

Wen, D.R., Liu, D.Y., Chung, S.L., Chu, M.F., Ji, J.Q., Zhang, Q., Song, B., Lee, T.Y., Yeh, M.W., Lo, C.H., 2008. Zircon SHRIMP U–Pb ages of the Gangdese Batholith and implications for Neotethyan subduction in southern Tibet. Chemical Geology 252, 191–201.

Winchester, J.A., Floyd, P.A., 1977. Geochemical discrimination of different magma series and their differentiation products using immobile elements. Chemical Geology 20, 325–343.

Windley, B.F., Alexeiev, D., Xiao, W.J., Kröner, A., Badarch, G., 2007. Tectonic models for accretion of the Central Asian Orogenic Belt. Journal of the Geological Society 164, 31–47.

Wu, H., Li, H.Q., Chen, F.W., Lu, Y.F., Deng, G., Mei, Y.P., Ji, H.G., 2006. Zircon SHRIMP U–Pb dating of plagiogranite porphyry in the Chihu molybdenum–copper district, Hami, East Tianshan. Geological Bulletin of China 25, 549–552 (in Chinese with English abstract).

Xia, L.Q., Xu, X.Y., Xia, Z.C., Li, X.M., Ma, Z.P., Wang, L.S., 2004. Petrogenesis of carboniferous rift-related volcanic rocks in the Tianshan, northwestern China. Geological Society of America Bulletin 116, 419–433.

Xia, L.Q., Xia, Z.C., Xu, X.Y., Li, X.M., Ma, Z.P., 2008. Relative contributions of crust and mantle to the generation of the Tianshan Carboniferous rift-related basic lavas, northwestern China. Journal of Asian Earth Sciences 31, 357–378.

Xiao, W.J., Santosh, M., 2014. The western Central Asian Orogenic Belt: a window to accretionary orogenesis and continental growth. Gondwana Research 25, 1429–1444.

Xiao, W.J., Zhang, L.C., Qin, K.Z., Sun, S., Li, J.L., 2004. Paleozoic accretionary and collisional tectonics of the eastern Tianshan (China): implications for the continental growth of central Asia. American Journal of Science 304, 370–395.

Xiao, W.J., Windley, B.F., Huang, B.C., Han, C.M., Yuan, C., Chen, H.L., Sun, M., Sun, S., Li, J.L., 2009. End-Permian to mid-Triassic termination of the accretionary processes of the southern Altaids: implications for the geodynamic evolution, Phanerozoic continental growth, and metallogeny of Central Asia. International Journal of Earth Sciences 98, 1189–1217.

Xiao, W.J., Huang, B.C., Han, C.M., Sun, S., Li, J.L., 2010. A review of the western part of the Altaids: a key to understanding the architecture of accretionary orogens. Gondwana Research 18, 253–273.

Xiao, W.J., Windley, B.F., Allen, M.B., Han, C.M., 2013. Paleozoic multiple accretionary and collisional tectonics of the Chinese Tianshan orogenic collage. Gondwana Research 23, 1316–1341.

Xiao, W.J., Han, C.M., Liu, W., Wan, B., Zhang, J.E., Ao, S.J., Zhang, Z.Y., Song, D.F., Tian, Z.H., Luo, J., 2014. How many sutures in the southern central Asian orogenic belt: insights from East Xinjiang–West Gansu (NW China)? Geoscience Frontiers 5, 525–536.

Xiao, W.J., Sun, M., Santosh, M., 2015. Continental reconstruction and metallogeny of the Circum-Junggar areas and termination of the southern Central Asian Orogenic Belt. Geoscience Frontiers 6, 137–140.

Xiong, X.L., 2006. Trace element evidence for growth of early continental crust by melting of rutile-bearing hydrous eclogite. Geology 34, 945–948.

Xu, J.F., Shinjo, R., Defant, M.J., Wang, Q., Rapp, R.P., 2002. Origin of Mesozoic adakitic intrusive rocks in the Ningzhen area of east China: partial melting of delaminated lower continental crust? Geology 30, 1111–1114.

Zhang, L.C., Xiao, W.J., Qin, K.Z., Zhang, Q., 2006. The adakite connection of the Tuwu–Yandong copper porphyry belt, eastern Tianshan, NW China: trace element and Sr–Nd–Pb isotope geochemistry. Mineralium Deposita 41, 188–200.

Zhang, L.C., Qin, K.Z., Xiao, W.J., 2008. Multiple mineralization events in the eastern Tianshan district NW China: isotopic geochronology and geological significance. Journal of Asian Earth Sciences 32, 236–246.

Zhang, D.Y., Zhou, T.F., Yuan, F., Fan, Y., Liu, S., Peng, M.X., 2010. Geochemical characters, metallogenic chronology and geological significance of the Yanxi copper deposit in eastern Tianshan, Xinjiang. Acta Petrologica Sinica 26, 3327–3338 (in Chinese with English abstract).

Zhao, Z.Y., Zhang, Z.C., Santosh, M., Huang, H., Cheng, Z.G., Ye, J.C., 2015. Early Paleozoic magmatic record from the northern margin of the Tarim Craton: further insights on the evolution of the Central Asian Orogenic Belt. Gondwana Research 28, 328–347.

Zhou, L.G., Xia, Q.X., Zheng, Y.F., Hu, Z.C., 2014. Polyphase growth of garnet in eclogite from the Hong'an orogen: constraints from garnet zoning and phase equilibrium. Lithos 206–207, 79–99.